

1 **The protocataclasite dilemma: *in situ* ³⁶Cl and REE-Y lessons from an impure limestone**
2 **fault scarp at Sparta, Greece**

3
4 Bradley W. Goodfellow^{1,2,3,4}, Marc W. Caffee^{5,6}, Greg Chmiel⁵, Ruben Fritzon^{1,3#}, Alasdair
5 Skelton^{2,3}, Arjen P. Stroeven^{1,3*}

6
7 ¹Department of Physical Geography, Stockholm University, Stockholm, Sweden

8 ²Department of Geological Sciences, Stockholm University, Stockholm, Sweden

9 ³Bolin Centre for Climate Research, Stockholm University, Stockholm, Sweden

10 ⁴Geological Survey of Sweden, Killiansgatan 10, Lund, Sweden

11 ⁵Department of Physics and Astronomy/Purdue Rare Isotope Measurement Laboratory,
12 Purdue University, West Lafayette, USA

13 ⁶Department of Earth, Atmospheric, and Planetary Sciences, Purdue University, West
14 Lafayette, USA

15
16 *Corresponding author

17 Email: arjen.stroeven@natgeo.su.se

18 Phone: +46(0)8-16 4230

19 #Now at Celsiusskolan, Sporthallsvägen 7, 828 33 Edsbyn, Sweden

20

21

22

23

24

25

26

27

28

29

30

31

32

33

34

35

36

37

38

39

40

41

42

43

44

45

46

47

48

49

50

51

52

53

54

55

56

57

58

59

60

Abstract

Reconstructions of paleoseismicity are useful for understanding, and mitigating, seismic hazard risks. We apply cosmogenic ³⁶Cl exposure-age dating and measurements of concentrations of rare-earth elements and yttrium (REE-Y) concentrations to the paleoseismic history of the Sparta Ffault, Greece. Bayesian-inference Markov chain Monte Carlo modeling of ³⁶Cl concentrations along a 7.2 m-long vertical profile on the Sparta Fault scarp at Anogia indicate an increase in average slip rate of the scarp from 0.8–0.9 mm yr⁻¹ at 6.5–7.7 kyr ago to 1.1–1.2 mm yr⁻¹ up to the devastating 464 B.C.E. earthquake. Average exhumation of the entire scarp up to the present day is 0.7–0.8 mm yr⁻¹. Modelling does not indicate additional recent exhumation of the Sparta Ffault after 464 B.C.E. The Sparta Ffault scarp is composed of fault breccia, containing quartz and clay-lined pores, in addition to host rock-derived clasts of calcite and microcrystalline calcite cement. The impurities control the distribution of REE-Y in the fault scarp surface and contribute spatial variation to ³⁶Cl concentrations, which precludes the identification of individual earthquakes that have exhumed the Sparta Ffault scarp from either of these data sets. REE-Y may illustrate processes that localize slip to a

37 discrete fault plane in the Earth's near-surface but their potential use in paleoseismicity
38 would benefit from further evaluation.

39

40 **Keywords**

41 ³⁶Cl exposure dating; [earthquake fault slip rate](#); limestone; normal fault; REE-Y; Sparta [F](#)fault

42

43 **1 Introduction**

44 Seismic hazard risks are significant in many parts of the world and studying the magnitude,
45 recurrence, mechanisms, and impacts of past earthquakes helps form a basis for mitigating
46 current and future risk. While historical earthquake records are a crucial archive (Gürpınar,
47 2005), their spatial distribution is patchy and the recurrence interval of large earthquakes on
48 many faults predates historical records. Geologic-based inferences regarding earthquake
49 timing, recurrence intervals, and the magnitudes of slip and shaking intensity, are an essential
50 component of seismic hazard risk mitigation (McCalpin, 2009, p. 24). Topographic
51 expressions of tectonic faults, the displacement of surficial sediments revealed in trenches,
52 and geochemical alterations on subaerially exposed fault surfaces, may each provide evidence
53 useful to the study of paleoseismicity (e.g., Benedetti et al., 2002; Dramis and Blumetti,
54 2005; Michetti et al., 2005; Carcaillet et al., 2008; Manighetti et al., 2010; Mouslopoulou et
55 al., 2011; [Smith et al., 2014](#); Cowie et al., 2017; Mozafari et al., 2022). Here we apply
56 concentrations of cosmic-ray-produced (cosmogenic) ³⁶Cl and rare-earth elements and
57 yttrium (REE-Y) to study paleoseismicity on the Sparta [F](#)fault at Anogia, Greece (Fig. 1a, b).

58

59 The Mediterranean is a densely populated seismically active region subjected to ~~7360~~
60 [hundreds of](#) earthquakes of magnitude (M) > 4 ~~during 1998–2010~~ [every year](#) (Godey et al.,
61 2013; [Meng et al., 2021](#); [Ozkula et al., 2023](#)). Within the Aegean tectonic plate (Fig. 1a),

62 and around its margins, there were >1450 earthquakes during ~~this period~~ 1998–2010 (Godey
63 et al., 2013), 77 of which were $M > 5$. In central Greece, earthquakes are associated with
64 normal faults, which occur because of extension of the Aegean plate (Jolivet et al., 2013). In
65 limestone, they may be identified by spectacular scarps, which form from the accumulation
66 of bedrock slip that occurs during successive earthquakes. Holocene fault scarps can be well-
67 preserved (Armijo et al., 1991), making them suitable targets for paleoseismic studies.

68

69 The concentration of cosmogenic ^{36}Cl (Zreda and Noller, 1998; Mitchell et al., 2001;
70 Benedetti et al., 2002; Palumbo et al., 2004; Schlagenhauf et al., 2010; Tesson et al., 2016;
71 Cowie et al., 2017; Iezzi et al., 2021; Mozafari et al., 2022) has been used to infer
72 paleoseismic activity in limestone normal faults. This nuclide is produced from spallogenic
73 and muonic reactions occurring in ^{40}Ca in limestone exposed at the surface and in the
74 uppermost few meters of the subsurface. Following an earthquake, the newly exposed scarp
75 segment accumulates ^{36}Cl , the concentration of which is dependent upon the duration of
76 subaerial exposure plus the preceding duration of subsurface exposure, potentially allowing
77 the earthquake to be dated. The higher the concentration of ^{36}Cl , the older the earthquake
78 which has exhumed the sampled scarp segment. Because the highest part of a scarp was
79 exhumed first, ages increase towards the top of a scarp.

80

81 Despite the potential for ^{36}Cl dating of earthquakes, a given ^{36}Cl concentration profile may
82 not have a unique tectonic reconstruction (Goodall et al., 2021). Scarp exhuming earthquakes
83 may be temporally clustered, making it challenging to resolve individual earthquakes within
84 the uncertainties of ^{36}Cl measurements (Bubeck et al., 2015). Also, ^{36}Cl concentrations along
85 vertical profiles that deviate from the theoretically predicted patterns ~~However, because~~
86 ~~earthquakes may be closely clustered in time (Bubeck et al., 2015) and the measured ^{36}Cl~~

87 concentrations may be consistent with a range of models (Goodall et al., 2021), a unique
88 unequivocal fit to a single model may not be possible. Fault scarps may be exhumed by
89 earthquakes clustered within several thousands of years and then lie dormant for similar, or
90 even longer, periods (Wallace, 1987; Friedrich et al., 2003; Benedetti et al., 2013, Cowie et
91 al., 2017). Accurately identifying individual earthquakes is further challenged by ³⁶Cl
92 concentrations along vertical profiles that deviate from the theoretically predicted patterns.
93 These deviations appear to be a ubiquitous feature of normal faults developed in limestone
94 (e.g., Benedetti et al., 2002; Palumbo et al., 2004; Tesson et al., 2016; Cowie et al., 2017;
95 Goodall et al., 2021; Mozafari et al., 2022; Dawood et al., 2024). Collectively, these These
96 challenges have ~~driven~~ helped motivate the development of ~~more sophisticated~~ probabilistic
97 models for determining exhumation histories from ³⁶Cl concentration profiles (Tikhomirov et
98 al., 2019). For example, Bayesian modeling incorporates prior geologic information
99 (Cowie et al., 2017; Beck et al., 2018; Tesson and Benedetti, 2019; ~~Tikhomirov et al., 2019;~~
100 Goodall et al., 2021, Iezzi et al., 2021) ~~with the goal of making more robust inferences about~~
101 ~~past tectonic activity~~ to identify the most probable exhumation history from complex ³⁶Cl data
102 and make inferences on the seismogenic potential of a fault (Tesson et al., 2016).
103
104 ~~Fault scarps may be exhumed by earthquakes clustered within several thousands of years and~~
105 ~~then lie dormant for similar, or even longer, periods (Wallace, 1987; Friedrich et al., 2003;~~
106 ~~Benedetti et al., 2013, Cowie et al., 2017).~~ Although this complicates the determination of
107 earthquake recurrence intervals, earthquake clusters followed by intervening quiescence may
108 may be discerned from fault scarp ³⁶Cl concentrations (Goodall et al., 2021). Exposure ages
109 from Holocene faults may provide information essential to determining the seismogenic
110 potential of a fault (Tesson et al., 2016).

111

112 Measurements of REE-Y have also been used to unravel paleoseismic information on
113 limestone fault scarps, frequently together with ^{36}Cl dating (Carcaillet et al., 2008; Manighetti
114 et al., 2010; Mouslopoulou et al., 2011; Tesson et al., 2016; Bello et al., 2023; Moraetis et al.,
115 2023). The distribution of REE-Y vertically along fault scarps may result from exchanges
116 with former hanging-wall soil REE-Y before uplift. REE-Y would be leached from
117 subaerially exposed scarp surfaces through calcite dissolution and accumulate in the surfaces
118 of ~~the~~ hanging wall soil where they form organic complexes (Carcaillet et al., 2008; Bello et
119 al., 2023; Moraetis et al., 2023). Because of low pH, calcite dissolution is highest where the
120 soil surface abuts the scarp and the REE-Y becomes locally enriched in the adjacent scarp
121 surface through soil-to-scarp REE-Y exchange during reprecipitation of calcite. Peaks in
122 REE-Y on fault scarp surfaces that are now ~~subaerially~~ subaerially exposed may therefore
123 represent former soil surfaces, which are now exposed to leaching and subsequent
124 accumulation in the hanging wall soil, thus completing a cycle. The spacing of these REE-Y
125 peaks may permit identification of the number of slip events and the vertical displacement
126 lengths. These inferences can be made independently of ^{36}Cl measurements. Using both
127 techniques could provide robust paleoseismic information for seismic risk assessment
128 models.

129

130 The pioneering cosmogenic ^{36}Cl study of the Sparta ~~F~~ fault by Benedetti et al. (2002)
131 motivated our studies. Benedetti et al. found evidence at Parori (Fig. 1b) for the historically
132 recorded 464 B.C.E. earthquake that destroyed Sparta (Armijo et al., 1991) and five older
133 earthquakes. Interestingly, they were unable to substantiate a displacement from the historical
134 464 B.C.E. earthquake at nearby Anogia. Our study objectives were to: (i) study slip rates on
135 the Sparta ~~F~~ fault at Anogia, by taking advantage of recent advances in both the measurement
136 of ^{36}Cl and earthquake modelling, accounting for all ^{36}Cl production pathways and shielding

137 effects (Schlagenhauf et al., 2010), and Bayesian modelling ~~using prior knowledge such as~~
138 ~~the 464 B.C.E. earthquake~~ (Goodall et al., 2021); and (ii) ~~c~~Complement the ^{36}Cl exposure
139 dating with measurements of REE-Y to best constrain the paleoseismic history of this fault.

140

141 **2 Geological Setting**

142 The Sparta ~~F~~fault is a 64 km long, NNW–SSE striking, range-bounding normal fault in
143 southern Peloponnese (Fig. 1a, b). It separates the eastern flank of the Taygetos Mountains
144 (maximum elevation of 2407 m a.s.l.) from the Sparta Basin (Fig. 1b). The Sparta ~~F~~fault is
145 part of a larger normal fault system, which exceeds 150 km in length, and is matched on the
146 western margin of the Taygetos Mountains by the antithetical Kalamata fault and other
147 similar faults located offshore of the Mani Peninsula (Fig. 1a; Armijo et al., 1991; Çal et al.,
148 2024). The subaerially exposed scarp of the Sparta ~~F~~fault is developed in late Senonian-
149 Eocene limestones of the Ionian unit (Institute for Geology and Subsurface Research, 1969;
150 Armijo et al., 1991). Folded and tilted Permian to early Triassic pelitic and psammitic
151 sedimentary and metasedimentary units outcrop in the Taygetos Mountains and are also
152 offset by the Sparta ~~F~~fault at depth (Institute for Geology and Subsurface Research, 1969;
153 Armijo et al., 1991). Geomorphic evidence for Quaternary uplift along the eastern flank of
154 the Taygetos Mountains includes steep triangular facets (20° – 40°) that are hundreds of
155 meters high along the central portion of the range and decrease in height towards the N and S,
156 wineglass canyons, perched valleys, ~~and~~ alluvial fans having up to 4 m of entrenchment near
157 the Sparta ~~F~~fault trace, and slope-break knickpoints (Armijo et al., 1991; Benedetti et al.,
158 2002; Pope and Wilkinson, 2005; Papanikolaou et al., 2013; Çal et al., 2024). Collectively,
159 the evidence indicates an environment that has been tectonically active during the Holocene.

160

161 The Sparta **F**fault scarp is nearly continuous along strike and it reaches a maximum height of
162 10–12 m in its central portion but tapers towards both ends. Hanging wall erosion associated
163 with stream incision can locally form higher scarp segments. The scarp has a 61–64° dip and,
164 in all but a few locations, slickensides have been eroded away following exhumation. The
165 slope of the hanging wall ground surface matches that upslope of the footwall, which
166 indicates a contiguous hillslope prior to formation of the present scarp and that sediment
167 accumulation at the scarp base is generally minor. Some wedges of sediment are locally
168 present on the hanging wall and in some places are welded to the scarp face, in positions now
169 perched above the hanging wall (Fig. S1). These wedges may have been perched by
170 earthquake-induced displacement on the Sparta **F**fault or are debris deposits from mass
171 movements that have partly eroded. It is possible that other sediment wedges were also
172 formerly attached to the scarp face but have since fallen off.

173
174 Our sampling site is located at Anogia, where the Sparta **F**fault scarp is 6.8 m high (Fig. 1c),
175 sparsely fractured, and displays a smooth surface texture (Fig. 1d-e). Apparent slickensides
176 are faintly visible as grooves that may have been widened and deepened by weathering, and
177 the surface displays a black coating, like those commonly occurring on limestone and which
178 contain higher concentrations of SiO₂ and Al₂O₃ than the underlying rock (Carcaillet et al.,
179 2008). The scarp surface at Anogia also displays a spatially variable distribution of subaerial
180 weathering features such as rills and dissolution pits, which we avoided in our sampling. The
181 lower-angle hillslopes on both the foot wall (above the fault scarp) and hanging wall display
182 a patchy distribution of bedrock outcrops and an indurated allochthonous regolith composed
183 of limestone clasts, with a matrix of red aeolian dust and calcite cement. An outcrop of
184 limestone about 50 m upslope of the fault scarp reveals folded and tilted bedding. The
185 bedding nearest to the scarp has a dip of 45–60° and a strike of 268–279°, which corresponds

186 with those for the fault scarp, indicating that faulting appears to exploit these structural
187 weaknesses in the bedrock. We neither observed scarps with a total offset of 2–3 m within
188 tens of meters downslope of the Sparta Ffault scarp (Benedetti et al., 2002), nor observed
189 fault scarps within hundreds of meters upslope of the Sparta Ffault scarp. If earthquakes,
190 including at 464 B.C.E., bypassed the fault scarp at Anogia (Benedetti et al., 2002), they did
191 not leave geomorphic expressions that we observed on field reconnaissance.

192

193

194 **3 Methods**

195 To study the paleoseismicity of the Sparta Ffault, we combined Accelerated Mass
196 Spectrometry (AMS) measurements of cosmogenic ^{36}Cl concentrations from samples
197 collected from the Sparta Ffault scarp with field and laboratory analyses of scarp composition
198 and mineralogy, and with field measurements of hanging wall soil composition and pH. We
199 made these measurements by sampling a vertical ^{36}Cl profile at Anogia, upwards from the
200 ground surface and adjacent to the sampling transect of Benedetti et al. (2002) for direct
201 comparison with that pre-existing record (Fig. 1c). We also took samples for ^{36}Cl and
202 mineralogical analyses, including REE-Y, from a second vertical profile located about 50 m
203 to the south (Fig. 1c). We chose this additional site for its smooth, non-fractured, fault scarp
204 surface, and sampling was completed from the top of the scarp to 80 cm below the present
205 ground surface, following hand excavation of a pit.

206

207 **3.1 ^{36}Cl concentrations**

208 We sampled the first profile (Anogia A), adjacent to the southern margin of the Benedetti et
209 al. (2002) profile, for ^{36}Cl by using an angle grinder to cut 10*20*3 cm ($h*w*d$) slabs from
210 the ground surface to a height of 3.9 m (Fig. 1c, d). Because of a crack in the fault scarp at

211 1.1 m above the ground, the transect was shifted laterally (towards the north) by 40 cm, thus
212 duplicating the measurement at 1.1 m. A total of 37 samples from this profile were measured
213 for ^{36}Cl concentration. We sampled the second profile (Anogia B), ~ 50 m further to the
214 south, for ^{36}Cl and mineralogical analyses initially by drilling 14 cores of 4 cm diameter to a
215 depth of 3 cm into the scarp surface (Fig. 1c, e). Four of these cores were spaced at 20 cm
216 intervals below the ground surface and eight were spaced at 80 cm intervals above the ground
217 surface to a height of 6.4 m, which is 0.4 m below the top of the scarp. These samples were
218 augmented by another two drill core samples at 1.2 m and at 6.0 m. Subsequently, we took 20
219 samples from this profile using an angle grinder to cut 10*20*3 cm ($h*w*d$) slabs from the
220 ground surface to a height of 2.0 m (Fig. 1c). A total of 71 samples from the three profiles
221 were subjected to preparation chemistry for ^{36}Cl targets and measured using AMS.

222

223 For ^{36}Cl measurements, limestone samples were crushed to approximately 0.5 mm diameter
224 and the whole sample was used without removing any size fraction through sieving. Prior to
225 partial dissolution approximately 120 g of crushed material was washed with deionized water
226 to remove fines. Following Stone et al. (1996), meteoric ^{36}Cl was removed using two cycles
227 of partial dissolution with nitric acid to dissolve 5% (by mass) of the carbonate each time. To
228 prepare the AMS target we used 30 g of dried sample, spiked with 1 mg of ^{35}Cl -enriched
229 sodium chloride carrier (Source: Icon Isotopes, ^{35}Cl 99.635 atom %, $^{35}\text{Cl}/^{37}\text{Cl} = 273$) to
230 measure native chloride by isotope dilution. A slurry of the sample and 120 g of deionized
231 water was slowly dissolved with 60 g of concentrated trace-metal grade nitric acid. Post-
232 dissolution, both liquid and undissolved solids were quantitatively transferred to a centrifuge
233 bottle where the solids were removed by centrifugation. The supernatant was decanted to
234 another centrifuge bottle and chloride was precipitated using one molar silver nitrate. After a
235 settling period, the bottle was centrifuged to isolate the silver chloride which was then

236 washed, dissolved with ammonium hydroxide, and treated with barium nitrate to remove
237 sulfate in preparation for further purification by chromatography. The solution was loaded
238 onto 5 ml of Bio-Rad AG 1-X8 strong anion-exchange resin and chloride was moved through
239 with 0.50 mmol, and then 0.150 mmol, nitric acid. After re-precipitation with silver nitrate
240 and a washing step the silver chloride was dried and packed into silver bromide-cored copper
241 holders. AMS measurements were performed at the Purdue Rare Isotope Measurement
242 Laboratory according to procedures in Muzikar et al. (2003); standards used for the
243 measurement are described in Sharma et al. (1990).

244

245 *3.1.1 Bayesian modelling of ^{36}Cl concentrations*

246 We apply the Bayesian Markov chain Monte Carlo (MCMC) code from Goodall et al. (2021)
247 to identify slip rates from ^{36}Cl concentrations. MCMC builds upon ‘modelscarp’ from
248 Schlagenhauf et al. (2010), which models the number of earthquakes, their ages, and resulting
249 displacements from ^{36}Cl concentrations based on user-defined inputs. ‘Modelscarp’ accounts
250 for each ^{36}Cl production pathway in limestone (Table 1 in Schlagenhauf et al., 2010). The
251 Goodall et al. (2021) MCMC code is adapted from Cowie et al. (2017) to generate potential
252 slip histories.

253

254 The MCMC code models: (i) scarp age, which is the timing of the earthquake to exhume the
255 uppermost, and therefore oldest, part of the fault scarp; (ii) time at which each subsequent
256 earthquake occurred and the corresponding height of exhumed scarp; and (iii) time since the
257 most recent earthquake exhumed the lowest part of the fault scarp (elapsed time). The
258 exhumation of the entire scarp is attributed to a user-defined number of earthquakes that each
259 exhumed the same vertical length of scarp. This constant length stipulation is a requirement
260 of the MCMC code and is acceptable because the MCMC code focusses on modelling slip

261 rates rather than identifying individual earthquakes, which is an appropriate methodology for
262 our ^{36}Cl data. The timing of each earthquake, apart from the first and last, is therefore
263 dependent on the selected number of earthquakes. We follow Goodall et al. (2021) in using
264 the flexible change point method of Cowie et al. (2017), which allows for variable slip rates
265 between iterations.

266

267 We parametrized the MCMC model as follows: (i) We defined the scarp age as a 1σ
268 normally distributed prior of 8000 years ~~with a 1σ normally distributed prior of 1500 years.~~

269 This selection is partly based on the record that contemporary faults scarps in the
270 Mediterranean region are Holocene in age. They have been exhumed since the last glacial
271 maximum (LGM) because hillslope bedrock erosion and regolith transport rates were much
272 higher during the LGM (e.g., more than ten times higher for the Magnola Fault in Italy;
273 Tucker et al., 2011), preventing ruptured fault scarps from persisting as subaerially exposed
274 features (e.g., Benedetti et al., 2002; Cowie et al., 2017; Goodall et al., 2021). The adopted
275 scarp age is refined ~~as a consequence of~~ through fitting a modelled ^{36}Cl concentration profile
276 to the measured ^{36}Cl concentration profile using the ‘modelscarp’ code of the MCMC model.
277 The scarp age is also balanced by the period of pre-exposure, which is the ^{36}Cl inventory that
278 accumulated in the bedrock while it was mantled by a up to a few meters of colluvium before
279 initial post-LGM subaerial exposure. A wide Gaussian prior (5000–16 000 years), is assigned
280 in our modeling to account for the uncertainty in scarp age. (ii) The elapsed time is defined as
281 2500 years, based on the youngest known earthquake on the Sparta Fault of 464 B.C.E. We
282 assign a 1σ uncertainty of 1000 years to reflect uncertainty in the historical record. (iii) To
283 further define the most likely slip rate history for the Sparta ~~F~~fault, we completed multiple
284 model runs with varying number of earthquakes (three to six) and ^{36}Cl spallation production
285 rates (48.8 ± 3.5 to 59.4 ± 4.3 atoms $\text{g Ca}^{-1} \text{yr}^{-1}$). These end-member production rates are

286 from Stone et al. (1996) and Schlagenhauf et al. (2010) ~~re-calculated from using~~ Lifton et al.,
287 (2005), respectively. All model runs used the temporally variable geomagnetic field of Lifton
288 et al. (2005) to scale the ^{36}Cl spallation production rate, and spallation production rates for K,
289 Ti, and Fe are as shown in Table 1 from Schlagenhauf et al. (2010). Scarp age and elapsed
290 time are the priors in the MCMC model, the number of earthquakes defines the timing and
291 location on the scarp of slip change points, and prior probabilities are as defined in the
292 Goodall et al. (2021) MCMC code.

293

294 The MCMC algorithm generates a slip history, using the input parameters conditioned on
295 prior probability, to construct a forward model of ^{36}Cl concentrations for this slip history
296 (Goodall et al., 2021). The quality of the slip history solution is then assessed by comparing
297 modelled and measured ^{36}Cl concentration profiles. The algorithm iteratively adjusts a
298 parameter defining the slip history and recalculates a new forward model solution.

299 Acceptance of the new slip history hinges on either its likelihood surpassing that of the prior
300 model or the ratio of new to current likelihood exceeding a randomly selected value from a
301 uniform distribution between zero and one. Otherwise, the new model solution is discarded,
302 adhering to the principles of the Metropolis-Hastings algorithm (Metropolis et al., 1953;
303 Hastings, 1970). We ran this process for 200 000 iterations, using the parameters in Table 1,
304 and results were assessed on 160 000 iterations-~~after following exclusion of~~ a burn-in phase
305 of 40 000 iterations ~~were excluded~~ to mitigate the influence of initial parameters.

306

307 **3.2 Sparta ~~F~~fault scarp composition**

308 Fault scarp chemical composition and mineralogy were analyzed from Anogia B as follows.

309 An initial elemental analysis was done in the field on the Sparta ~~F~~fault scarp surface using an
310 Olympus Innov-X Delta (40 kV) handheld X-ray fluorescence (XRF) device. This instrument

311 performs elemental analyses with a circular sample spot of 8 mm diameter and can measure
312 elements heavier than Na. All elements lighter than Mg are reported as lighter elements (LE).
313 Of the elements that compose REE-Y, it was only capable of measuring yttrium. Sampling
314 was done at an interval of 5 cm (or less) over a 7.7 m vertical profile, beginning ~0.9 m
315 below the hanging wall soil surface. This profile corresponds with the location of the drill
316 core and 2.0 m-long ^{36}Cl profiles at Anogia B but was measured before either drilling or slab
317 sampling (Fig. 1c).

318

319 For more detailed analyses of elements, including REE-Y, a total of 39 cores (22 mm and 35
320 mm diameters and to depths of ~3 cm) were collected every 20 cm from a vertical transect at
321 Anogia B using a portable drill (Fig. 1d). The outermost 1 mm was removed from each core
322 prior to crushing to avoid contamination from the black surface coating. The next 15 mm of
323 each core were then rinsed with cold water, air dried, and crushed using a grinder with a steel
324 mortar to a grain size of $<100\ \mu\text{m}$. This crushing technique might supply additional REE-Y to
325 samples (Hickson and Juras, 1986) but if so, this likely occurs systematically across samples
326 and we are more interested in spatial trends, which we confirm independently using the
327 handheld XRF, than absolute abundances. The crushed samples were then analyzed for major
328 and trace elements using fusion inductively coupled plasma mass spectrometry (FUS-ICP-
329 MS) at Activation Laboratories (Ontario, Canada).

330

331 We complemented the FUS-ICP-MS analyses with spot elemental analysis of one rock core
332 from 1.1 m above the scarp base at Anogia B to make a high-resolution determination of any
333 spatial variations in the scarp composition. This was done with an energy-dispersive X-ray
334 spectroscope (EDS) attached to an environmental scanning electron microscope (ESEM). We
335 used a Quanta FEG 650 with Oxford-Inka EDS, and the analysis was made in a high-vacuum

336 environment at 20 kV. The technique is incapable of detecting REE-Y because their
337 concentrations are too low. Photomicrographs and backscatter images of pore spaces were
338 also taken using the ESEM. These analyses were completed at the Department of Geological
339 Sciences, Stockholm University.

340

341 **3.3 Sparta Ffault scarp mineralogy**

342 A modal analysis of mineral fractions was completed on thin sections taken from the
343 remaining 38 core samples. This was done by counting 1000 points on each thin section
344 (Hutchison, 1974) using a Pelcon automatic point counter attached to a Leica (DM LSP)
345 optical microscope. This point counter comprises a stepping frame attached to a control box
346 (power supply) and is also connected to a computer for statistical analyses using Pelcon
347 software version 2. The point counting and mineral identification was made using an
348 objective working distance of 1.52 mm. The line section pre-set step-length was 0.3 mm and
349 the line section distance was 1.5–2 mm. The point counting permitted a detailed quantitative
350 analysis of the mineralogy of the Sparta Ffault scarp surface. This detailed mineralogy was
351 then compared with the chemical composition data to determine whether phases other than
352 the host limestone are present.

353

354 **3.4 Hanging wall soil chemistry and pH**

355 Soil chemistry and pH were measured in samples taken at ~10 cm intervals to a depth of ~90
356 cm in the pit excavated at the base of the Anogia B profile (Fig. 1c). The elemental analysis
357 was again done with the handheld XRF device. Indicator strips were used to measure pH
358 from mixtures of 1:1 mass ratio of soil:distilled water, and soil:1 M KCl (Sikora and Moore,
359 2014). These analyses help determine the vertical distribution of REE-Y in the soil (using

360 yttrium as a proxy) and indicate how they might correlate with pH and the vertical
361 distribution of REE-Y in the fault scarp below the soil surface.

362

363 4 Results

364 4.1 Sparta ~~F~~fault ³⁶Cl concentrations

365 The cosmogenic nuclide ³⁶Cl concentrations from our three profiles (Table S1) and the
366 original Benedetti et al. (2002) ³⁶Cl concentrations are compared in Figure 2. The Anogia A
367 and Anogia B profiles display corresponding trends of increasing ³⁶Cl concentrations with
368 increasing height on the fault scarp. Only at 1.6 m do the trends strongly deviate from each
369 other. The Anogia B profile indicates generally lower ³⁶Cl concentrations including six of 19
370 points that do not overlap within uncertainty with data points at corresponding elevations on
371 the Anogia A profile. Four of those points are located from 1.0 m to 1.3 m. In comparison
372 with Anogia A, the adjacent segment of the Benedetti et al. (2002) profile (0–4 m) shows ³⁶Cl
373 concentrations that are on average 19% higher. Uncertainties (1σ) for data points comprising
374 each profile are almost identical, displaying a mean of 3.8% for the Benedetti et al. (2002)
375 profile versus 3.9% for the Anogia A and Anogia B profiles. However, the Benedetti et al.
376 (2002) profile displays more variation between adjacent sample points than is evident in our
377 profiles. Whereas concentrations differ between the three longest profiles, they show a
378 consistent gradient up to ~4 m on the scarp. Above 4 m on the scarp, both our Anogia B drill-
379 core profile and the Benedetti et al. (2002) profile display matching lower gradients. Whereas
380 differences in measured concentrations between our two profiles and the Benedetti et al.
381 (2002) profile might be expected given technical advances between measurements,

382 ~~successive samples in our data display inconsistent variations between~~ the Anogia A and B
383 profiles do not mirror each other, despite them being horizontally separated by only ~ 50 m.

384 This inability to consistently replicate measurements along the two ~~adjacent~~ profiles justifies

385 a focus on identifying slip rates using the Goodall et al. (2021) model, rather than individual
386 earthquakes, also because up-scarp ^{36}Cl concentration gradients are more consistent between
387 the profiles.

388

389 Slip rates for the Sparta ~~F~~fault are explored through comparing scarp exhumation generated
390 by three, five, and six modelled earthquakes, where each earthquake exhumes 183 cm, 122
391 cm, and 104 cm, respectively (calculated by dividing the scarp height by the number of
392 model earthquakes). We focus our analyses on the Anogia A profile supplemented with drill
393 core samples from above 3.9 m on the scarp and from the scarp surface buried by colluvium.

394 This combined profile was chosen for modelling both because the Anogia A profile was
395 sampled at 10 cm intervals up to 3.9 m on the scarp, versus only 2.1 m for Anogia B, and
396 because Anogia A is located adjacent to the Benedetti et al. 2002 profile. Furthermore,
397 MCMC modelling of ^{36}Cl concentrations did not converge with measured concentrations for
398 the full Anogia B profile (i.e., including the drill core samples above 2.1 m), but rather only
399 for the intensively sampled lowermost 2.1 m plus subsurface drill core samples. Modelling
400 only the lowermost 2.1 m plus subsurface drill core samples necessitated changes to scarp
401 age and preexposure from those used for the Anogia A plus drill core sample profile, because

402 this lowermost part of the scarp has a younger age, and to slip length because the 2.1 m
403 profile length is indivisible into the 6.5 m length of the Anogia A plus drill core sample
404 profile. These changes, especially to scarp age, invalidate comparisons of slip rates between

405 the two profiles, ~~which are the focus of this paper.~~ We did not measure compositions for the
406 Anogia A samples, so we use a mean scarp composition from Anogia B in our modelling.

407 Results from the Goodall et al. (2001) model applied to the Anogia A plus drill core profile
408 are shown below and in Figure S2, respectively, for end-member ^{36}Cl production rates of

409 $59.4 \pm 4.3 \text{ atoms g Ca}^{-1} \text{ yr}^{-1}$ ~~from Schlagenhauf et al. (2010) calculated from Lifton et al.,~~

410 ~~(2005)~~ and 48.8 ± 3.5 atoms g Ca⁻¹ yr⁻¹ ~~from Stone et al. (1996).~~ Geochemical data for the
411 fault scarp used in modelling are shown in Table S2. Modelling results from Anogia B
412 (lowermost 2.1 m and subsurface drill core samples and the entire profile) are shown in
413 Figure S3.

414

415 The results of the Bayesian inference MCMC modelling of ³⁶Cl data from the Sparta ~~F~~ fault
416 are shown in Figures 3–5. The accepted scarp exhumation models (n = 160 000) are shown in
417 slip versus time histograms (Fig. 3a). The maximum a posteriori probability (MAP) model,
418 shown by the red line, deviates slightly from the maximum model density (mean model,
419 black line) for each slip segment, but more so for the slip segment at 4.9–6.1 m on the scarp.
420 It indicates three exhumation events between 2.4 and 6.1 m on the scarp, that are closely
421 spaced in time at 5000–6000 years ago. The 95% confidence intervals (Fig. 3b) illustrate little
422 change in variance between model results from lower, younger parts of the scarp to older,
423 higher parts of the scarp, although the MAP model deviates towards being younger than the
424 mean model towards the top of the scarp. The range of accepted models fits the measured
425 ³⁶Cl data well (Fig. 3c) but accommodates a broad range of corresponding slip histories along
426 the entire vertical length of the scarp (Fig. 3d).

427

428 Statistics for how well the MCMC modelling fits the measured ³⁶Cl data and our initial
429 estimates of scarp age (8000 years) and elapsed time (2500 years) are illustrated in Figure 4
430 and summarized in Table S2. The posterior probability distribution function indicates that the
431 elapsed time since the most recent earthquake is consistent with the 464 B.C.E. earthquake
432 (mean of 2501 ± 164 – 173 years; Fig. 4a; [Table S2](#)). In contrast, the time when the scarp
433 started to form (scarp age), presumably through a decrease in hillslope erosion following the
434 LGM, is indicated by the posterior probability distribution to have been longer than our initial

435 estimate of 8000 years (mean of 8742 ± 502 years; Fig. 4b; [Table S2](#)). Mean values of
436 likelihood, weighted mean root square (RMS_w) and corrected Akaike's Information Criterion
437 (AICc) are 0.25–0.28, 13.9–14.6, and 863–893, respectively, across the ~~modelled~~-range of the
438 ~~modelled~~ number of slip events (Figs. 4d and 4e; Table S2), indicating that the number of
439 earthquakes (change points) has minor influence on modelling a fit to measured ^{36}Cl
440 concentrations.

441

442 The slip rate for the Sparta Fault is calculated from the most probable of models (i.e., the top
443 6.25% of fits to the ^{36}Cl data ($n = 10\,000$); Fig. 5, Table 2). For the entire vertical length of
444 the fault scarp, and five modelled earthquakes, both the mean and MAP slip rates are 0.7–0.8
445 mm yr^{-1} for end-member ^{36}Cl production rates, calculated up to the present day (Fig. 5a). For
446 the same calculation but excluding the 2500 year since the most recent known earthquake at
447 464 B.C.E., the slip rates are higher, with mean and MAP values of 1.1 and 1.2 mm yr^{-1} ,
448 respectively (Fig. 5b). The lowest 3.7 m of the fault scarp is the most recently exhumed scarp
449 segment and the most intensively sampled. It displays a steep ^{36}Cl concentration gradient,
450 which indicates matching mean and MAP slip rates of 1.0 mm yr^{-1} , for five model
451 earthquakes (Fig. 5c). The highest 2.5 m of the scarp displays a gentler ^{36}Cl concentration
452 gradient relative to the bottom 3.9 m of the scarp as indicated by our drill core samples and
453 the Benedetti et al. (2002) profile. The mean and MAP slip rates for this scarp segment are
454 therefore lower, at 0.8–0.9 mm yr^{-1} (Fig. 5d). Varying the number of earthquakes between
455 three and six has minor influence on the calculated slip rates (Table 2). An increase in mean
456 slip rate occurred between 6.7 and 5.3 kyr (Fig. 5e).

457

458 **4.2 Granulometry of the Sparta ~~F~~fault scarp surface**

459 A first look at the Sparta **F**fault scarp surface yields a misleading impression of homogeneous
460 limestone (Figs. 1, 6a), whereas close inspection of the core samples instead reveals a typical
461 fault breccia (Figs. 6b-d). This breccia consists of angular-to-rounded limestone clasts with
462 axes of 1–7 mm (in the two-dimensional view provided by thin sections) surrounded by
463 matrix/cement in which clasts are <0.1 mm in length. The fault breccia is defined as a
464 protocataclasite, according to the classification of Woodcock and Mort (2008). The
465 composition of the protocataclasite displays large spatial variations, with some portions
466 containing abundant clasts (Fig. 6c), whereas others are dominated by fine matrix (Fig. 6d).
467 The proportion of clasts >2 mm ranges from 5% to 20% vertically along the fault scarp and
468 the proportion of matrix ranges from 5% to 60%. We did not measure the thickness of the
469 protocataclasite but it everywhere exceeds the 3 cm depth of our drill cores.

470

471 **4.3 Sparta **F**fault scarp composition and mineralogy**

472 In addition to a spatially variable granulometry, the fault scarp shows a spatially variable
473 distribution of major and trace elements. The major component is, as expected for limestone,
474 CaO (mean 52.22%) but its concentration varies between 43.83% and 56.64% (Table S3),
475 which exceeds spatial variations in CaO seen elsewhere in limestone normal fault scarps
476 (Carcaillet et al., 2008; Tesson et al., 2016). Quartz (SiO₂) also occurs, and it too displays
477 spatial variations (0.10%–20.82%), with broad peaks occurring at 0.5–0.4 m below the
478 ground, and 0.9–1.2 m, 4.6–4.8 m, and 6.0–6.2 m along the vertical fault scarp profile (Fig. 7;
479 Table S3). An additional peak in SiO₂, but which is not seen in point counting of quartz,
480 occurs at 6.62 m (Fig. 7; Tables S3 and S4). The point counting and geochemical
481 measurements were done on different aliquots of the sample slab extracted from each level,
482 thereby causing variation in quartz concentration between the two methods, which is
483 prominent at 6.6 m. Mean concentrations of other major elements are low in bulk samples,

484 including Al₂O₃ (0.21%), MgO (0.16%), Fe₂O₃ (0.09%), P₂O₅ (0.07%), and K₂O (0.05%;
485 Table S3). However, EDS measurements, such as shown in Figure 8a, reveal that the
486 concentrations of some elements are frequently much higher in intergranular pores (Fig. 8c)
487 than elsewhere in the fault scarp, including Si ≤ 38.3%, Al ≤ 11.7%, Fe ≤ 48.4%, and K ≤
488 7.1% (Table S5). Furthermore, intergranular pores and quartz frequently occur together (Fig.
489 8b) and the concentration of Al₂O₃ covaries with the much more abundant quartz (SiO₂) (Fig.
490 7).

491

492 Quartz is revealed by microscopy to be present as randomly oriented rounded-to-angular
493 grains that are <50 μm in diameter (Figs. 6d, 8b). Quartz is a constituent of the
494 protocataclasite fine matrix that is mostly comprised of microcrystalline calcite precipitates
495 and which cements larger host rock-derived CaCO₃ clasts (Figs. 6b-d, 8b, 9a). Point counting
496 further reveals quartz modes ranging from 0.1% to 15.4% of thin section area (Table S4),
497 with higher abundances correlating to higher abundances of fine matrix. The spatial
498 correlations between SiO₂, quartz abundances on point counting, and fine matrix are further
499 strengthened by EDS spot elemental analyses (Fig. 9). Here, the two selected spots in the fine
500 matrix display Si abundances of 29.7% and 28.9%, which contrasts with 1.7% and 0.9% for
501 the two spots located on clasts. CaO abundances display an inverse relationship with SiO₂
502 (33.7% and 31.2% for the clasts versus 4.8% and 5.1% for the fine matrix). SiO₂ is present
503 largely as quartz, as evidenced by the strong spatial correlation between quartz and SiO₂
504 along the vertical profile (Fig. 7). Quartz can therefore be used as a proxy for fine matrix
505 abundances in the Sparta ~~F~~fault scarp.

506

507 In addition to the spatial relationship between quartz and fine matrix, we observed in
508 backscatter SEM images that pore spaces, which frequently harbor higher concentrations of

509 Si, Al, K and/or Fe than host rock-derived clasts, are also more abundant in the fine matrix
510 (Fig. 8c). These observations provide evidence that clay particles (< μm-scale) frequently
511 coat pore spaces. The abundance of quartz therefore also provides a proxy for the abundance
512 of clay-coated pore spaces.

513

514 Concentrations of REE-Y vary in a wave-like pattern along the vertical profile, with maxima
515 occurring at -0.4 m, 0.8 m, 2.6 m, 4.0 m, and 6.4 m (Y = 1.2–11.1 ppm; Table S6; Fig. 10).
516 These maxima do not systematically decrease with vertical distance above the hanging wall
517 and are not highest in the soil-mantled portion of the scarp. Yttrium (mean 6.3 ppm), La
518 (mean 5.04 ppm), Nd (mean 3.54 ppm), and Ce (mean 2.31 ppm) have the highest
519 concentrations, whereas all other REE-Y are <1 ppm (Table S6). The concentrations of REE-
520 Y elements co-vary vertically along the scarp surface ($R^2 = 0.95$; Fig. 10a).

521

522 There is no depletion of light (LREE) relative to heavy (HREE) rare-earth elements with
523 increasing height on the subaerially exposed fault scarp, where it ranges between 3.9 and 5.1
524 (Figs. 10b, 11a, Table S6). However, there is a relative depletion of LREE on the scarp
525 surface buried by soil (LREE/HREE is 3.2 to 4.0; Figs. 10b, 11a), with least depletion at 0.40
526 m depth and progressively larger LREE depletion with increasing depth. Peaks and troughs in
527 the LREE/HREE ratio along the vertical profile poorly match peaks and troughs in REE-Y
528 concentrations (Figs. 10a, b), although local minima correspond at 3 m and at 5.2 m on the
529 scarp. Accordingly, the correlation between LREE/HREE and total REE-Y concentration is
530 only weak ($R^2 = 0.36$; Fig. 11b).

531

532 REE-Y concentration maxima occur at locations that correspond closely with the Al_2O_3
533 maxima (Fig. 10a; Table S6). Accordingly, LREE, HREE, and total REE-Y are strongly

534 correlated with Al_2O_3 ($R^2 = 0.92$; Figs. 11c, S3a). Spatial correlations between REE-Y and
535 SiO_2 and K_2O are also observed ($R^2 = 0.56$ and 0.87 , respectively; Fig. S4c, e). Whereas
536 REE-Y concentrations vary in wave-like pattern along the scarp, REE-Y is not enriched, and
537 LREE is depleted relative to HREE, in the soil-covered scarp surface.

538

539 **4.4 Hanging wall soil chemistry and pH**

540 The terra rosa soil mantling the hanging wall primarily comprises aeolian dust (Muhs et al.,
541 2010) and carbonate clasts. At our sample site, the soil thickness at the base of the Sparta
542 **F**fault scarp is 0.8 m and this appears to be stable, at least over the timescale of scarp surface
543 dissolution, as evidenced by a much smoother scarp surface texture below the soil surface
544 compared with the subaerially exposed scarp. Below the organic horizon (~0.1 m thick) the
545 soil is welded, probably by calcite precipitates, and horizons are absent. Soil pH is, in
546 general, slightly acidic along the excavated vertical profile, remaining within a 6.2 to 7.0
547 range (Fig. 12a; Table S7). An outlier occurs at -0.30 m, where the pH is 5.6 ± 0.2 . Soil
548 composition varies with depth (Fig. 12b; Table S8). Concentrations of Si, Al, and K are lower
549 in the organic horizon (11%, 0–5%, and 0.4%, respectively) compared with the remainder of
550 the profile (18%–30%, 5–10%, and 0.5–0.9%, respectively), whereas the concentrations of
551 LE, which includes C, are, as expected, higher in the organic horizon (75%–80%) than in the
552 lower profile segment (51%–64%). The concentration of yttrium ranges from a maximum of
553 36–39 ppm at 0.5–0.6 m depth to a minimum of 11 ppm at 0.1 m depth and its vertical
554 distribution correlates positively with Si ($R^2 = 0.71$), Al ($R^2 = 0.45$), and K ($R^2 = 0.54$), and
555 negatively with pH ($R^2 = -0.52$; Figs. 12c, S4b,d,f; Table S8).

556

557 **5 Discussion**

558 **5.1 Slip rate on the Sparta Fault at Anogia**

559 The average exhumation rate of the entire scarp up to the present day is 0.7– 0.8 mm yr⁻¹
560 (Fig. 5a; Table 2). This compares with an exhumation rate of 1.1–1.2 mm yr⁻¹ up to the 464
561 B.C.E. earthquake (if an earthquake occurred now, the rate up to the present day would
562 increase). These values compare favorably with estimates of 0.8 mm yr⁻¹ and 1 mm yr⁻¹ from
563 Papanikolou et al (2013) and Benedetti et al. (2002), respectively, but are higher than the 0.5
564 mm yr⁻¹ exhumation rate estimated for the northernmost segment of the Sparta Fault (Çal et
565 al., 2024). Our data show an increase in average slip rate during exhumation of the scarp
566 from an initial 0.8–0.9 mm yr⁻¹ between 6.5 and 7.7 kyr ago to 1.0 mm yr⁻¹ between 3.0 and
567 6.0 kyr ago (Fig. 5e). These slip rates directly reflect the steeper ³⁶Cl gradient for the lower
568 4.0 m of the fault scarp compared with the gentler gradient from 4.0 to 6.5 m (Figs. 2 and 3c).
569 Although the sampling density is highest over the lowermost 4 m, we have confidence in the
570 lower inferred average slip rate for the higher, older part of the scarp because both our
571 dispersed drill core samples and the Benedetti et al. (2002) profile indicate a lower ³⁶Cl
572 concentration gradient (in trend, rather than absolute values) above 4 m. The MAP model
573 (Fig. 3a) indicates that three scarp exhuming earthquakes may have occurred during 5000-
574 6000 years ago (MAP average slip rate of 1.1 mm yr⁻¹), which is consistent with an increase
575 in average slip rate during this period observed in the slip rate versus time plot (Fig. 5e). The
576 lower rate of exhumation for the upper ~2.5 m reflects an apparent quiescent period prior to
577 these earthquakes. Neither the historical record nor the ³⁶Cl concentrations measured on the
578 Anogia A and B profiles (Figs. 3 and 4a), supported by measurements of geometry and
579 hanging wall colluvium, and in Benedetti et al. (2002) provide evidence for large, scarp-
580 exhuming, earthquakes after the 464 B.C.E. event. MCMC modelling does not indicate that
581 earthquakes have contributed to exhumation of the Sparta fault more recently than the last
582 historically recorded event at 464 B.C.E. Fault scarps may be exhumed by earthquakes
583 clustered within several thousands of years, and then lie dormant for similar, or even longer,

584 periods (Wallace, 1987; Friedrich et al., 2003; Benedetti et al., 2013, Cowie et al., 2017).

585 ~~Periods of quiescence appear to characterize normal faults in the Mediterranean region~~

586 ~~(Cowie et al., 2017; Goodall et al., 2021) and so t~~The recent 2.5 kyr period of quiescence is

587 therefore not necessarily indicative that another earthquake is imminent.

588

589 Our data do not uniquely specify the number and timing of scarp exhumation events and we

590 have been unable to identify other faults along the eastern flank of the Taygetos Mountains

591 suitable for ^{36}Cl analyses that with the Sparta Ffault may form part of a system, across which

592 slip is distributed. We therefore limit our interpretations to averaged slip rates and the timing

593 of changes in these rates for the Sparta Ffault at Anogia, rather than attempting to identify

594 individual earthquakes or draw conclusions on regional fault kinematics and associated

595 seismic hazards.

596

597 **5.2 Methodological and geological sources of uncertainty in the ^{36}Cl data**

598 A feature of the ^{36}Cl data is that our Anogia A and B profiles display systematically lower

599 concentrations than the Benedetti et al. (2002) profile (Fig. 2). The Benedetti et al. (2002)

600 profile also displays variations between adjacent sample points that exceed those observed in

601 our profiles. We interpret the systematic differences in ^{36}Cl concentration between our

602 profiles and the Benedetti et al. (2002) profile as reflecting methodological differences

603 related to advances in sample preparation chemistry at PRIME-Lab, Purdue University. For

604 this reason, we elect not to model the Benedetti et al. (2002) data using the MCMC

605 methodology.

606

607

608

609 Whereas our Anogia A and B profiles display corresponding trends with increasing elevation
610 on the fault scarp, Anogia B samples have generally lower ^{36}Cl concentrations (Fig. 2).
611 Indeed, six of its 19 ^{36}Cl concentrations do not overlap within uncertainty with concentrations
612 of corresponding samples on the 3.9 m Anogia A profile, including four points located
613 between 1.0 m and 1.3 m. We interpret these differences as indicating that the fault scarp at
614 Anogia B has been either partly shielded from cosmogenic radiation, has eroded more than
615 the scarp surface at Anogia A, or contains a higher concentration of non-calcite impurities
616 ([Section 5.3](#)). Of potential additional relevance is that the texture of the scarp surface at
617 Anogia B is smoother than at the location of Anogia A. Because a similarly smooth texture
618 also characterizes ~~the a portion of the~~ scarp surface presently buried by colluvium mantling
619 the hanging wall, the smooth texture at the location of Anogia B may indicate either recent
620 burial of the scarp surface by colluvium and/or CaCO_3 dissolution/reprecipitation occurring
621 at a higher rate than at locations where the exposed scarp surface texture is rougher. If a
622 smooth texture reflects erosion through CaCO_3 dissolution, there might be preferential flow,
623 or seepage, of water from the hillslope above the scarp at the location of Anogia B. Observed
624 lumps of colluvium cemented to the Sparta ~~F~~fault scarp, at locations perched above the
625 present hanging wall surface (Fig. S1) partially shield the underlying scarp surface today.
626 However, had this previously occurred at the location of Anogia B, an eroded colluvial lump
627 would be evidenced in the hanging wall sediments. On the contrary, there is no colluvial
628 lump, but rather a sub-horizontal surface is present with an expression that differs little from
629 the surface below the Anogia A profile. The inter-profile differences in ^{36}Cl concentrations
630 illustrate the value in taking samples for ^{36}Cl measurements from more than one vertical
631 profile at a particular location, because ^{36}Cl concentrations can vary either through spatial
632 variations in non-calcite impurities or past shielding by sediments or bedrock, which can

633 otherwise be difficult to detect. Partial shielding may impact the interpretation of
634 paleoseismicity, including the timing, number and magnitudes of earthquakes, through
635 locally lowered ^{36}Cl concentrations.

636

637 **5.3 The effects of mineralogical impurities on ^{36}Cl concentrations**

638 Mineralogical impurities embedded in the fault breccia that comprise the scarp surface appear
639 to be a key geological reason for spatial variations in the concentration of ^{36}Cl . Measurements
640 of chemistry and mineralogy at Anogia B indicate that SiO_2 comprises 0.1–20.8 wt.% of the
641 scarp. Because the concentration of CaCO_3 is inversely correlated with SiO_2 (largely quartz),
642 then peaks in SiO_2 might coincide with troughs in ^{36}Cl , although a simple relationship
643 vertically along the scarp is obscured by the relationship between ^{36}Cl concentration and
644 exposure duration. A local peak in SiO_2 of 12–15 wt.% coincides with a local low in ^{36}Cl
645 concentration at Anogia B between about 0.6 and 1.2 m on the scarp (Figs. 2 and 7, Tables S1
646 and S3). A distinct low in ^{36}Cl concentration at 1.6 m also corresponds with a local peak in
647 SiO_2 of 9 wt.%. However, the magnitudes of the variations are inconsistent between these
648 two locations, such that a high peak in SiO_2 corresponds with a small reduction of ^{36}Cl at
649 0.6–1.2 m and vice versa at 1.6 m. Because ^{36}Cl is also produced by spallation on K ($162 \pm$
650 24 atoms $\text{g}^{-1} \text{yr}^{-1}$ at SLHL; Evans et al., 1997), Fe (1.3 ± 0.1 atoms $\text{g}^{-1} \text{yr}^{-1}$ – 1.9 ± 0.2 atoms g^{-1}
651 yr^{-1} at SLHL; Stone, 2005; Moore and Granger, 2019), and Ti (13 ± 3 atoms $\text{g}^{-1} \text{yr}^{-1}$ at
652 SLHL; Fink et al., 2000), noise in the ^{36}Cl data might also partly reflect the relative
653 abundances of these elements. However, this appears to be insignificant given that measured
654 concentrations of these elements are extremely low (concentrations of K_2O , Fe_2O_3 , and TiO_2
655 are 0–0.12%, 0.03–0.24%, and 0–0.02%, respectively; Fig. S4, Table S3). Other elements,
656 seemingly present as trace amounts of clay, lining pores in the fault breccia (Fig. 7, Table
657 S3), are also an insignificant contributor to variations in ^{36}Cl concentrations. For the Sparta

658 Ffault at Anogia, quartz embedded in the fault breccia may be the key mineralogical impurity
659 that is likely contributing variance to the ³⁶Cl concentrations, which in turn impacts our
660 ability to obtain unequivocal dates of individual earthquakes.

661

662 **5.4 Interpretation of REE-Y distributions and implications for paleoseismicity**

663 REE-Y cannot be used to infer imprints of former soil profiles on the Sparta Ffault at Anogia.
664 Petrographic analyses indicate that the Sparta Ffault scarp is composed of a protocataclasite
665 consisting of calcite clasts derived from the host limestone, microcrystalline calcite cement,
666 and quartz (Figs. 6, 7). Furthermore, EDS analysis indicates that trace amounts of clay, such
667 as illite, are lining pores where microcrystalline calcite cement and quartz are located (Fig. 8;
668 Carcaillet et al., 2008). We infer that REE-Y are adsorbed onto clay minerals lining pores in
669 the fine-grained matrix of the fault breccia, as indicated by correlations between REE-Y and
670 each of Al, K, Si, and Fe ($R^2 = 0.92, 0.87, 0.56, \text{ and } 0.47$, respectively; Fig. S4a-c) and
671 between Y and both Si and Al in the hanging wall colluvium ($R^2 = 0.71 \text{ and } 0.45$,
672 respectively; Figs. 12c and S4b,c). Supplementary data from the Kaparelli fault ($R^2 = 0.95$ for
673 Si; Figs. 1a and S5a) and Magnola fault hanging walls ($R^2 = 0.98$ for both Si and Al; Fig.
674 S5b,c and electronic appendix to Manighetti et al., 2010) also indicate REE-Y may be
675 adsorbed to clay embedded in limestone fault scarps. These correlations generally contrast
676 with a weaker negative correlation between Y and pH ($R^2 = 0.52$) for the hanging wall soil on
677 the Sparta Fault (Fig. 12c). Soil pH does not appear to be the dominant control on REE-Y
678 distributions in the Sparta Ffault scarp, which differs to interpretations on other limestone
679 fault scarps (Carcaillet et al., 2008; Bello et al., 2023).

680

681 We propose a causative relationship between the vertical distributions of REE-Y and clay on
682 the Sparta Ffault scarp. This reasoning is supported by the following observations:

- 683 (i) The Sparta Ffault scarp REE-Y concentrations are equivalent to (Nuriel et al.,
684 2012; Goodfellow et al., 2017) or higher than those measured elsewhere in
685 platformal limestone (Carcaillet et al., 2008; Mouslopoulou et al., 2011), but Y
686 concentrations are lower in the adjacent hanging wall soil (REE were not
687 measured in the soil; Tables S6, S8).
- 688 (ii) If REE-Y exchange between the soil and fault scarp occurs according to the
689 Carcaillet et al. (2008) model, fractionation of LREE and HREE elements is
690 expected. For example, LREE might be preferentially mobilized (Takahashi et al.,
691 2005; Carcaillet et al., 2008), leading to an enrichment of LREE relative to HREE
692 in the fault scarp, where there are peaks in total REE-Y. Conversely, LREE may
693 be depleted relative to HREE where there are troughs in total REE-Y. However,
694 the proportion of LREE to HREE remains confined to a constant range vertically
695 along the subaerial section of Sparta Ffault scarp (Figs.10b, 11a), is weakly
696 correlated with total REE-Y ($R^2 = 0.36$; Fig. 11b), and is relatively depleted at all
697 measured depths beneath the soil surface (Fig. 10b).
- 698 (iii) There is no systematic decrease with distance above the hanging wall in total
699 REE-Y (Fig. 10a, b), in contrast to declining concentrations with distance above
700 the hanging wall on the Magnola fault (Carcaillet et al., 2008).

701 Adsorption of REE-Y onto clay has been observed in regolith (Borst et al., 2020) but has not
702 been previously discussed in the context of interpreting paleoseismicity on limestone fault
703 scarps.

704

705 Although we infer that adsorption of REE-Y onto clay minerals embedded in fault breccia
706 dominates on the Sparta Ffault, the approximate coincidence of the subsurface peak in scarp
707 LREE/HREE and total REE-Y with the mid-profile peak in soil pH (Figs. 10, 12a, b)

708 provides evidence of REE-Y exchange between the scarp and the soil. However, the
709 consequence is LREE depletion in the scarp, rather than enrichment (Fig. 10b), and it is
710 unclear why this apparent depletion is not replicated on the subaerially exposed scarp. One
711 possibility is that colluvium accumulation postdates the most recent earthquake although, if
712 so, low ^{36}Cl concentrations in the buried scarp surface indicate that the soil accumulation was
713 co-seismic with the last earthquake or accumulated soon afterwards. It is also unclear why
714 colluvium would accumulate only after the most recent earthquake. An alternative possibility
715 is that a superficial LREE-depleted zone has been eroded from the subaerial scarp surface
716 through dissolution. This would imply erosion of centimeters of scarp surface since the last
717 known earthquake on the Sparta ~~F~~fault at 464 B.C.E. (an erosion rate of 0.01 mm yr^{-1} over
718 the past 2500 years would remove 2.5 cm of scarp surface). Yet another possibility is that
719 perhaps more time is required to increase LREE to concentrations seen on the subaerial scarp
720 surface, but 2500 years have already passed since the most recent known earthquake and
721 maximum REE-Y enrichment has been inferred to occur within 500 years on the Spilli and
722 Magnola faults (Manighetti et al., 2010; Mouslopoulou et al., 2011). Alternatively, LREE
723 enrichment occurs after scarp exhumation, perhaps through exchange with aeolian dust
724 fallout, as has been observed in Dead Sea halite (Censi et al., 2023). Such dust inputs may
725 supply REE-Y (Yang et al., 2007), as indicated by the correlation between Y and Si in the
726 hanging wall colluvium (Fig. 12b, c), contribute fine-grained mineral soil to the hanging wall
727 colluvium, and may lower soil pH through buffering locally-sourced CaCO_3 . However, given
728 that inputs of Saharan dust are ubiquitous throughout the Mediterranean (Stuut et al., 2009)
729 and can comprise a large component of soils in the region (Muhs et al., 2010; Styllas et al.,
730 2023), similar patterns of LREE depletion in the soil-covered scarp surface relative to the
731 subaerial scarp surface are expected to have been observed elsewhere, which is not the case

732 (Carcaillet et al., 2008; Manighetti et al., 2010; Mouslopoulou et al., 2011; Tesson et al.,
733 2016; Bello et al., 2023).

734

735 For the Sparta Ffault scarp, the presence of clay likely relates to fault breccia formation at
736 considerable depths beneath the Earth's surface, rather than subaerial weathering processes.

737 The formation of protocataclasite occurs beneath the Earth's surface at depths that may range

738 from meters to up to thousands of meters. A model for this involves fluids moving along the

739 Sparta Ffault, primarily associated with seismic events. These fluids dissolve CaCO₃ from the
740 host-limestones and potentially also silicate minerals from psammitic and pelitic

741 (meta)sediments, where they are dissected by the fault. In association with variations in

742 temperature and pressure along the fault, chemical saturation of these fluids results in

743 precipitation of clay, quartz, and microcrystalline calcite, which cements clasts of host-rock

744 derived limestone into the fault breccia. Subsequent faulting re-fractures the breccia and

745 particle comminution over time produces quartz grains that are rounded-to-angular in shape,

746 randomly oriented, and <50 μm (Figs. 6, 8). The fault breccia may also have undergone

747 multiple generations of microcrystalline calcite re-cementing from re-circulating fluids. As an

748 alternative to a dissolution-precipitation model, clay and quartz emplacement may involve

749 fluid entrainment of particles and grains from clay- and quartz-bearing sedimentary units

750 during faulting, as has been observed elsewhere (e.g., Darwin, 1840; Roy, 1946; Brandon,

751 1972; Röshoff and Cosgrove, 2002). This process may also be accompanied by comminution

752 of fault-zone quartz grains derived from psammitic rocks. We tentatively exclude a

753 contemporary aeolian source for the clay and quartz because there is no documented

754 mechanism to transport clay particles and quartz grains from the soil to centimeters into a

755 fault scarp. We cannot distinguish soil to scarp clay and quartz migrations on the Sparta

756 Ffault which has been observed, for example, at the micrometer scale in surface coatings on

757 the Magnola fault, because that scarp is comprised of pure carbonate (Carcaillet et al., 2008).
758 It is likely that limestone fault scarps are generally composed of fault breccias (Agosta and
759 Aydin, 2006; Carcaillet et al., 2008; Nuriel et al., 2012) and that where a fault intersects
760 varying lithologies, chemical and mineralogical heterogeneities may occur in the fault
761 breccia, as observed on the Sparta Ffault. Where they occur, these heterogeneities may
762 control the spatial distribution of REE-Y, independent of any spatial reorganization of REE-
763 Y attributable to subaerial weathering. If, as we infer, the spatial patterning of REE-Y, quartz,
764 and clay is inherited from depth, the observed wave-like signal (Figs. 7, 10) may reflect
765 sorting and cementing of breccia around surface asperities on the fault plane. The resulting
766 infilling of depressions with fault gouge may create a successively more polished and
767 localized fault plane along which friction is lowered, thereby permitting larger slip (i.e.,
768 larger earthquakes) along the fault (Sagy and Brodsky, 2009). Whereas REE-Y
769 concentrations do not appear to be a reliable indicator of Holocene paleoseismicity of the
770 Sparta Ffault, they may instead reveal processes that localize slip to a discrete fault plane.
771
772 Whereas the Sparta Fault displays concentrations of clay and quartz impurities that are much
773 higher than on other reported limestone fault scarps, three general implications emerge for
774 using REE-Y in making inferences of paleoseismicity. Firstly, the potential control on REE-
775 Y distributions of even trace amounts of non-calcite impurities in the breccia comprising fault
776 scarps should be considered through analyses of thin sections in addition to scarp chemistry.
777 Secondly, soil acidity and REE-Y enrichment, including any resulting exchange with the
778 buried scarp, may peak some tens of centimeters below the colluvium surface. Peaks in REE-
779 Y concentrations on subaerial fault scarp surfaces may not therefore reflect former soil
780 surfaces, even if there is soil-scarp exchange of REE-Y. In addition, the Sparta Ffault scarp
781 REE-Y data indicate that it may be rewarding to focus on up-scarp variations in LREE/HREE

782 ratios rather than on REE-Y concentrations, because these may be a sensitive indicator of
783 REE-Y exchange processes occurring beneath soil covers (Fig 10b). Lastly, relationships
784 between REE-Y distributions and soil mineralogy should be more closely assessed, in
785 addition to the commonly modelled and studied effects of pH (e.g., Carcaillet et al., 2008;
786 Manighetti et al., 2010; Mouslopoulou et al., 2011; Moraetis et al., 2015, 2023; Tesson et al.,
787 2016; Bello et al., 2023). Fine grained mineral inputs through aeolian dust fallout comprise
788 substantial volumes of Mediterranean soils (Muhs et al., 2010; Styllas et al., 2023). These
789 inputs may be complemented in the eastern Mediterranean by Holocene tephra from the
790 South Aegean Active Volcanic Arc or volcanic centers in Italy (Bourne et al., 2010; Smith et
791 al., 2011; Koutrouli et al., 2018; Vougioukalakis et al., 2019). ~~and~~ ~~d~~ Decadal to millennial
792 variations in Holocene dust and tephra fluxes may directly impact on REE-Y distributions in
793 hanging wall soils and potentially in scarp surfaces, in locations where soil-scarp REE-Y
794 exchange is important. These fluctuations may contribute to REE-Y patterns in soils that are
795 difficult to predict and in scarp surfaces reflect (volcanic, climatic, and pedogenic) processes
796 that may complicate potential paleoseismic inferences.

797

798 Moraetis et al. (2023) consider REE-Y analyses an established method in paleoseismicity.
799 Our detailed study errs towards caution; there remain important uncertainties regarding
800 processes of REE-Y enrichment and depletion in limestone fault scarps. Indeed, we maintain
801 that there is considerable uncertainty regarding how the resulting patterns should be
802 interpreted with respect to paleoseismicity. Fundamentally, it remains unclear how far into
803 buried scarp surfaces the REE-Y can be adsorbed from soil or incorporated into calcite
804 through dissolution-precipitation. A dissolution rate of 0.001 mm yr^{-1} will erode 1 cm from a
805 subaerially exposed scarp surface over 10 000 years, which is about the timescale considered
806 to be relevant to assessing full seismic cycles and therefore making accurate assessments of

807 paleoseismicity (Mouslopoulou et al., 2012; Tesson et al., 2016). Even such a slow rate of
808 subaerial scarp dissolution will therefore remove any REE-Y signals inherited from former
809 soil cover unless that exchange extends to centimeters into the scarp.

810

811 **6 Conclusion**

812 Modelling of slip rates from ^{36}Cl data from the Sparta Ffault at Anogia, Greece, indicates an
813 increase in average slip rate during exhumation of the scarp from 0.8–0.9 mm yr⁻¹ between
814 7.7 and 6.5 kyr ago to 1.0 mm yr⁻¹ between 6.5 and 2.5 kyr ago (the timing oif the historie
815 464 B.C.E. earthquake). Average exhumation of the entire scarp is 0.7– 0.8 mm yr⁻¹.

816 Earthquake ages were not modelled from our data, but there is no indication from our
817 analyses that earthquakes may have contributed to exhumation of the Sparta Fault since 464
818 B.C.E..Modelling does not indicate that earthquakes may have contributed to exhumation of
819 the Sparta fault since 464 B.C.E.

820

821 The Sparta Ffault scarp is impure; it is composed of fault breccia, which contains quartz and
822 clay-lined pores in addition to calcite. The vertical distribution of REE-Y is highly correlated
823 with the pore-clay and may indicate processes that localize slip to a discrete fault plane deep
824 below the ground surface. The potential exchange of REE-Y between the hanging wall
825 colluvium and the adjacent footwall scarp is overwhelmed at this site by REE-Y attached to
826 the pore clays inherited from depth. Because of this, Holocene earthquakes and their slip
827 distances and magnitudes cannot be inferred for the Sparta Ffault from REE-Y
828 concentrations. Whereas this is probably true also for similar impure limestone fault scarps
829 elsewhere, other controls on REE-Y distributions, in addition to hanging wall soil pH, should
830 be evaluated in attempting paleoseismic inferences more generally from normal fault scarps
831 developed in limestone.

833 **Author contribution**

834 AS and APS conceived the study and acquired the funding for RF. BWG, APS, and AS
 835 supervised RF. APS, AS, BWG, MWC, and RF participated in fieldwork. RF conducted the
 836 analysis of scarp composition and made initial interpretations. ~~BWG performed additional
 837 analyses and earthquake modelling, and wrote the manuscript.~~ GC led the laboratory
 838 preparation of samples for ^{36}Cl measurement, together with BWG, and calculated ^{36}Cl
 839 concentrations from the AMS data. BWG performed additional analyses and earthquake
 840 modelling, and wrote the manuscript. All authors contributed to data interpretation and
 841 manuscript editing.

842

843 **Competing interests**

844 Arjen P. Stroeven is a member of the editorial board for Solid Earth.

845

846 **Acknowledgements**

847 We thank Mikael Amlert for his assistance with field safety and sampling, Giorgos Maneas,
 848 station manager of the Navarino Environmental Observatory (NEO), for his extensive
 849 assistance with field logistics, and our deceased friend/colleague, Dan Zetterberg, Department
 850 of Geological Sciences, Stockholm University, for his assistance with thin section
 851 preparations. We further thank Alessandro Maria Michetti, Nasim Mozafari, and two
 852 anonymous reviewers for constructive criticism that improved this manuscript, and Federico
 853 Rossetti for editorial handling. This project was funded by the Stockholm University
 854 Research School for teachers focusing on Natural Hazards financed by the Swedish Research
 855 Council and by a grant from NEO. We gratefully acknowledge funding for fieldwork from
 856 the Swedish Society for Anthropology and Geography Andréé Fund to Fritzon.

857

858 **References**

- 859 Agosta, F. and Aydin, A.: Architecture and deformation mechanism of a basin bounding
 860 normal fault in Mesozoic platform carbonates, central Italy. *Journal of Structural
 861 Geology*, 28, 1445–1467, 2006.
- 862 Armijo, R., Lyon-Caen, H., and Papanastassiou, D.: A possible normal-fault rupture for the
 863 464 BC Sparta earthquake. *Nature*, 351, 137–139, 1991.
- 864 Beck, J., Wolfers S., and Roberts, G.P.: Bayesian earthquake dating and seismic hazard
 865 assessment using chlorine-36 measurements (BED v1). *Geoscience Model Development*,
 866 *11*, 4383–4397, 2018.
- 867 Bello, S., Perna, M.G., Consalvo, A., Brozzetti, F., Galli, P., Cirillo, D., Andrenacci, C.,
 868 Tangari, A.C., Carducci, A., Menichetti, M., Lavecchia, G., Stoppa, F., and Rosatelli, G.:
 869 Coupling rare earth element analyses and high-resolution topography along fault scarps to
 870 investigate past earthquakes: A case study from the Southern Apennines (Italy).
 871 *Geosphere*, 19, 1348–1371, 2023.
- 872 Benedetti, L., Finkel, R., Papanastassiou, D., King, G., Armijo, R., Ryerson, F., Farber, D.,
 873 and Flerit, F.: Post-glacial slip history of the Sparta fault (Greece) determined by ^{36}Cl
 874 cosmogenic dating: Evidence for non-periodic earthquakes. *Geophysical Research
 875 Letters*, 29, 1246, 2002.
- 876 Benedetti, L., Manighetti, I., Gaudemer, Y., Finkel, R., Malavieille, J., Pou, K., Arnold, M.,
 877 Aumaître, G., Bourlès, D. and Keddadouche, K.: Earthquake synchrony and clustering on
 878 Fucino faults (Central Italy) as revealed from in situ ^{36}Cl exposure dating. *Journal of
 879 Geophysical Research, Solid Earth*, 118, 4948–4974, 2013.

- 880 Borst, A. M., Smith, M. P., Finch, A. A., Estrade, G., Villanova-de-Benavent, C., Nason, P.,
881 Marquis, E., Horsburgh, N. J., Goodenough, K. M., Xu, C., Kynický, J. and Geraki,
882 K.: Adsorption of rare earth elements in regolith-hosted clay deposits. *Nature*
883 *Communications*, 11, 4386, 2020.
- 884 [Bourne, A.J., Lowe, J.J., Trincardi, F., Asioli, A., Brockley, S.P.E., Wulf, S., Matthews, I.P.,](#)
885 [Piva, A., and Vigliotti, L., 2010. Distal tephra record for the last ca 105,000 years from](#)
886 [core PRAD 1-2 in the central Adriatic Sea: implications for marine tephrostratigraphy.](#)
887 [Quaternary Science Reviews, 29, 3079–3094, 2010.](#)
- 888 Brandon, A: Clastic dykes in the Namurian shales of County Leitrim, Republic of Ireland.
889 *Geological Magazine*, 109, 361–367, 1972.
- 890 Bubeck, A., Wilkinson, M., Roberts, G. P., Cowie, P. A., McCaffrey, K. J. W., Phillips, R.
891 and Sammonds, P.: The tectonic geomorphology of bedrock scarps on active normal
892 faults in the Italian Apennines mapped using combined ground penetrating radar and
893 terrestrial laser scanning. *Geomorphology*, 237, 38–51, 2015.
- 894 [Çal, Ç., Boulton, S.J., and Mildon, Z., Structural and geomorphological constraints on the](#)
895 [activity of the Sparta Fault \(Greece\). *Journal of the Geological Society* 181, 2024.](#)
896 [https://doi.org/10.1144/jgs2024-066.](https://doi.org/10.1144/jgs2024-066)
- 897 Carcaillet, J., Manighetti, I., Chauvel, C., Schlagenhauf, A., and Nicole, J.-M.: Identifying
898 past earthquakes on an active normal fault (Magnola, Italy) from the chemical analysis of
899 its exhumed carbonate fault plane. *Earth and Planetary Science Letters*, 271, 145–158,
900 2008.
- 901 Censi, P., Sirota, I., Zuddas, P., Lensky, N.G., Crouvi, O., Cangemi, M. and Piazzese, D.:
902 Rare earths release from dissolving atmospheric dust and their accumulation into
903 crystallising halite: The Dead Sea example. *Science of the Total Environment*, 875,
904 162682, 2023.
- 905 Cowie, P.A., Phillips, R.J., Roberts, G.P., McCaffrey, K., Zijerveld, L.J.J., Gregory, L.C.,
906 Faure Walker, J., Wedmore, L.N.J., Dunai, T.J., Binnie, S.A., Freeman, S.P.T.H.,
907 Wilcken, K., Shanks, R.P., Huismans, R.S., Papanikolaou, I., Michetti, A.M. and
908 Wilkinson, M.: Orogen-scale uplift in the central Italian Apennines drives episodic
909 behaviour of earthquake faults. *Scientific Reports*, 7, 44858, 2017.
- 910 Darwin, C: Geological observations in the volcanic islands and parts of South America
911 visited during the voyage of H.M.S. Beagle. London, 1840.
- 912 Dawood, R., Matmon, A., Benedetti, L., ASTER Team and Siman-Tov, S.: Multi-segment
913 earthquake clustering as inferred from ³⁶Cl exposure dating, the Bet Kerem fault system,
914 northern Israel. *Tectonics*, 43, e2023TC007953, 2024.
- 915 Dramis, F, and Blumetti, A.M.: Some considerations concerning seismic geomorphology and
916 paleoseismology. *Tectonophysics*, 408, 177–191, 2005.
- 917 Evans, J.M, Stone, J.O.H., Fifield, L.K., and Cresswell, R.G.: Cosmogenic chlorine-36
918 production in K-feldspar. *Nuclear Instruments and Methods in Physics Research B*, 123,
919 334–340, 1997.
- 920 Fink, D., Vogt, S., and Hotchkis, M.: Cross-sections for ³⁶Cl from Ti at E_p = 35–150 MeV:
921 Applications to in-situ exposure dating. *Nuclear Instruments and Methods in Physics*
922 *Research B*, 172, 861–866, 2000.
- 923 Friedrich, A. M., Wernicke, B. P., Niemi, N. A., Bennett, R.A. and Davis, J.L.: Comparison
924 of geodetic and geologic data from the Wasatch region, Utah, and implications for the
925 spectral character of Earth deformation at periods of 10 to 10 million years, *Journal of*
926 *Geophysical Research: Solid Earth*, 108, 2199, 2003.
- 927 Godey, S., Bossu, R., and Guilbert, J.: Improving the Mediterranean seismicity picture thanks
928 to international collaborations. *Physics and Chemistry of the Earth, Parts A/B/C*, 63, 3–
929 11, 2013.

- 930 Goodall, H. J., Gregory, L. C., Wedmore, L. N. J., McCaffrey, K. J. W., Amey, R. M. J.,
931 Roberts, G. P., Shanks, R.P., Phillips, R.J. and Hooper, A. Determining histories of slip
932 on normal faults with bedrock scarps using cosmogenic nuclide exposure data. *Tectonics*,
933 40, e2020TC006457, 2021.
- 934 Goodfellow, B.W., Viola, G., Bingen, B., Nuriel, P. and Kylander-Clark, A.: Paleocene
935 faulting in SE Sweden from U-Pb dating of slickenfiber calcite. *Terra Nova*, 29, 321–328,
936 2017.
- 937 Gürpinar, A.: The importance of paleoseismology in seismic hazard studies for critical
938 facilities. *Tectonophysics*, 408, 23–28, 2005.
- 939 Hastings, W.K.: Monte Carlo sampling methods using Markov chains and their applications.
940 *Biometrika*, 57, 97–109, 1970.
- 941 Hickson, C.J. and Juras, S.J.: Sample contamination by grinding. *Canadian Mineralogist*, 24,
942 585–589, 1986.
- 943 Hutchison, C.S.: *Laboratory Handbook of Petrographic Techniques*. Wiley-Interscience, New
944 York, 527 pp, 1974.
- 945 Iezzi, F., Roberts, G., Faure Walker, J., Papanikolaou, I., Ganas, A., Deligiannakis, G., Beck,
946 J., Wolfers, S. and Gheorghiu, D.: Temporal and spatial earthquake clustering revealed
947 through comparison of millennial strain-rates from ³⁶Cl cosmogenic exposure dating and
948 decadal GPS strain-rate. *Scientific Reports*, 11, 23320, 2021.
- 949 Institute for Geology and Subsurface Research: Sparti Sheet, photogeological map of Greece,
950 1969.
- 951 Jolivet, L., Faccenna, C., Huet, B., Labrousse, L., Le Pourhiet, L., Lacombe, O., Lecomte, E.,
952 Burov, E., Denèle, Y., Brun, J.-P., Philippon, M., Paul, A., Salaün, G., Karabulut, H.,
953 Piromallo, C., Monié, P., Gueydan, F., Okay, A.I., Oberhänsli, R., Pourteau, A., Augier,
954 R., Gadenne, L. and Driussi, O.: Aegean tectonics: Strain localisation, slab tearing and
955 trench retreat. *Tectonophysics*, 597–598, 1–33, 2013.
- 956 [Koutrouli, A., Anastasakis, G., Kontakiotis, G., Ballengee, S., Kuehn, S., Pe-Piper, G., and](#)
957 [Piper, D.J.W.: The early to mid-Holocene marine tephrostratigraphic record in the](#)
958 [Nisyros-Yali-Kos volcanic center, SE Aegean Sea. *Journal of Volcanology and*](#)
959 [Geothermal Research](#), 366, 96–111, 2018.
- 960 Lifton, N.A., Bieber, J.W., Clem, J.M., Duldig, M.L., Evenson, P., Humble, J.E. and Pyle, R.:
961 Addressing solar modulation and long-term uncertainties in scaling secondary cosmic
962 rays for in situ cosmogenic nuclide applications. *Earth and Planetary Science Letters*,
963 239, 140–161, 2005.
- 964 ~~Lifton, N.A., Sato, T. and Dunai, T.J.: Scaling in situ cosmogenic nuclide production rates~~
965 ~~using analytical approximations to atmospheric cosmic ray fluxes. *Earth and Planetary*~~
966 ~~*Science Letters*, 386, 149–160, 2014.~~
- 967 ~~Lifton, N.A., Smart, D.F. and Shea, M.A.: Scaling time integrated in situ cosmogenic nuclide~~
968 ~~production rates using a continuous geomagnetic model. *Earth and Planetary Science*~~
969 ~~*Letters*, 268, 190–201, 2008.~~
- 970 Manighetti, I., Boucher, E., Chauvel, C., Schlagenhauf, A. and Benedetti, L.: Rare earth
971 elements record past earthquakes on exhumed limestone fault planes. *Terra Nova*, 22,
972 477–482, 2010.
- 973 Marrero, S.M., Phillips, F.M., Caffee, M.W. and Gosse, J.C.: CRONUS-Earth cosmogenic
974 ³⁶Cl calibration. *Quaternary Geochronology*, 31, 199–219, 2016.
- 975 McCalpin, J.P.: *Paleoseismology*, Academic press, 613 pp., 2009.
- 976 McDonough, W.F. and Sun, S.-s.: The composition of the Earth. *Chemical Geology*, 120,
977 223–253, 1995.
- 978 [Meng, J., Sinoplu, O., Zhou, Z., Tokay, B., Kusky, T., Bozkurt, E., and Wang, L.: Greece and](#)
979 [Turkey shaken by African tectonic retreat. *Scientific Reports* 11, 6486, 2021.](#)

980 Metropolis, N., Rosenbluth, A. W., Rosenbluth, M. N., Teller A. H. and Teller, E.: Equation of state
981 calculations by fast computing machines. *Journal of Chemical Physics*, 21, 1087–1092, 1953.

982 Michetti, A.M., Audemard, F.A. and Marco, S.: Future trends in paleoseismology: Integrated
983 study of the seismic landscape as a vital tool in seismic hazard analyses *Tectonophysics*,
984 408, 3–21, 2005.

985 Mitchell, S.G., Matmon, A., Bierman, P.R., Enzel, Y., Caffee, M. and Rizzo, D.:
986 Displacement history of a limestone normal fault scarp, northern Israel, from cosmogenic
987 ³⁶Cl. *Journal of Geophysical Research: Solid Earth*, 106, 4247–4264, 2001.

988 Moore, A. K. and Granger, D. E.: Calibration of the production rate of cosmogenic ³⁶Cl from
989 Fe. *Quaternary Geochronology*, 51, 87–98, 2019.

990 Moraetis, D., Mouslopoulou, V., Pratikakis, A., Begg J. and Pracejus, B.: The mechanism of
991 REE-Y impregnation on active carbonate normal fault scarps. *Applied Geochemistry*,
992 155, 105703, 2023.

993 Mouslopoulou, V., Moraetis, D. and Fassoulas, C.: Identifying past earthquakes on carbonate
994 faults: Advances and limitations of the ‘Rare Earth Element’ method based on analysis of
995 the Spili Fault, Crete, Greece. *Earth and Planetary Science Letters*, 309, 45–55, 2011.

996 Mouslopoulou, V., Nicol, A., Walsh, J.J., Begg, J.G., Townsend, D.B. and Hristopulos, D.T.:
997 Fault-slip accumulation in an active rift over thousands to millions of years and the
998 importance of paleoearthquake sampling, *Journal of Structural Geology*, 36, 71–80, 2012.

999 Mozafari, N., Özkaymak, C., Sümer, Ö, Tikhomirov, D., Uzel, B., Yeşilyurt, S., Ivy-Ochs, S.,
1000 Vockenhuber, C., Sözbilir, H. and Akçar, N.: Seismic history of western Anatolia during
1001 the last 16 kyr determined by cosmogenic ³⁶Cl dating. *Swiss Journal of Geosciences*, 115,
1002 5, 2022.

1003 Muhs, D.R., Budahn, J., Avila, A., Skipp, G., Freeman, J. and Patterson, D.: The role of
1004 African dust in the formation of Quaternary soils on Mallorca, Spain and implications for
1005 the genesis of Red Mediterranean soils. *Quaternary Science Reviews*, 29, 2518–2543,
1006 2010.

1007 Muzikar, P., Elmore, D. and Granger, D.E.: Accelerator mass spectrometry in geologic
1008 research. *Geological Society of America Bulletin*, 115, 643–654, 2003.

1009 Nuriel, P., Rosenbaum, G., Zhao, J.-X., Feng, Y., Golding, S.D., Villemant, B. and
1010 Weinberger, R.: U-Th dating of striated fault planes. *Geology*, 40, 647–650, 2012.

1011 [Ozkula, G., Dowell, R.K., Baser, T., Lin, J.-L., Numanoglu, O.A., Ilhan, O., Olgun, C.G.,](#)
1012 [Huang, C-W., and Uludag, T.D.: Field reconnaissance and observations from the](#)
1013 [February 6, 2023, Turkey earthquake sequence. *Natural Hazards*, 119, 663–700, 2023.](#)

1014 Palumbo, L., Benedetti, L., Bourlès, D., Cinque, A. and Finkel, R.: Slip history of the
1015 Magnola fault (Apennines, Central Italy) from ³⁶Cl surface exposure dating: evidence for
1016 strong earthquakes over the Holocene. *Earth and Planetary Science Letters*, 225, 163–
1017 176, 2004.

1018 Papanikolaou, I.D., Roberts, G.P., Deligiannakis, G., Sakellariou, A. and Vassilakis, E.: The
1019 Sparta Fault, Southern Greece: From segmentation and tectonic geomorphology to
1020 seismic hazard mapping and time dependent probabilities. *Tectonophysics*, 597–598, 85–
1021 105, 2013.

1022 Pope, R.J. and Wilkinson, K.N.: Reconciling the roles of climate and tectonics in Late
1023 Quaternary fan development on the Spartan piedmont, Greece. In: A.M. Harvey, A.E.
1024 Mather, and M. Stokes, (Eds), *Alluvial Fans: Geomorphology, Sedimentology,*
1025 *Dynamics*. Geological Society, London, Special Publications, 251, 133–152, 2005.

1026 Röshoff, K. and Cosgrove, J.: Sedimentary dykes in the Oskarshamn-Västervik area. A study
1027 of the mechanism of formation. SKB Report R-02-37, 98 pp, 2002.

1028 Roy, C.J.: Clastic dykes of the Pikes Peak region. Abstract. *Geological Society of America*
1029 *Bulletin*, 57, 1226, 1946.

- 1030 Sagy, A. and Brodsky, E.E.: Geometric and rheological asperities in an exposed fault zone.
1031 Journal of Geophysical Research, 114, B02301, 2009.
- 1032 Schlagenhaut, A., Gaudemer, Y., Benedetti, L., Manighetti, I., Palumbo, L.,
1033 Schimmelpfennig, I., Finkel, R. and Pou, K.: Using *in situ* Chlorine-36 cosmnuclide to
1034 recover past earthquake histories on limestone normal fault scarps: a reappraisal of
1035 methodology and interpretations. Geophysical Journal International, 182, 36–72, 2010.
- 1036 Sharma, P., Kubik, P.W., Fehn, U., Gove, H.E., Nishiizumi, K. and Elmore, D.: Development
1037 of ³⁶Cl Standards for AMS. Nuclear Instruments & Methods in Physics Research Section
1038 B-Beam Interactions with Materials and Atoms, 52, 410–415, 1990.
- 1039 Sikora, F.J. and Moore, K.P. (Eds.): Soil Test Methods from the Southeastern United States.
1040 Southern Cooperative Series Bulletin, 419, 211 p., 2014.
- 1041 [Smith, V.C., Isaia, R., and Pearce, N.J.G.: Tephrostratigraphy and glass compositions of post-](#)
1042 [15 kyr Campi Flegrei eruptions: implications for eruption history and chronostratigraphic](#)
1043 [markers. Quaternary Science Reviews, 30, 3638–3660, 2011.](#)
- 1044 Stone, J.O.: Air pressure and cosmogenic isotope production. Journal of Geophysical
1045 Research: Solid Earth, 105, 23753–23759, 2000.
- 1046 Stone, J.O.: Terrestrial chlorine-36 production from spallation of iron. In: Abstract of 10th
1047 International Conference on Accelerator Mass Spectrometry, Berkeley, California, USA.,
1048 2005.
- 1049 Stone, J.O., Allan, G.L., Fifield, L.K. and Cresswell, R.G.: Cosmogenic chlorine-36 from
1050 calcium spallation. Geochimica et Cosmochimica Acta, 60, 679–692, 1996.
- 1051 Stuut, J.-B., Smalley, I. and O’Hara-Dhand, K.: Aeolian dust in Europe: African sources and
1052 European deposits. Quaternary International, 198, 234–245, 2009.
- 1053 Styllas, M., Pennos, C., Persoiu, A., Godelitsas, A., Papadopoulou, L., Aidona, E.,
1054 Kantiranis, N., Ducea, M.N., Ghilardi, M. and Demory, F.: Aeolian dust accretion
1055 outpaces erosion in the formation of Mediterranean alpine soils. New evidence from the
1056 periglacial zone of Mount Olympus, Greece. Earth Surface Processes and Landforms, 48,
1057 3003–3021, 2023.
- 1058 Takahashi, Y., Chatellier, X., Hattori, K.H., Kato, K. and Fortin, D.: Adsorption of rare earth
1059 elements onto bacterial cell walls and its implication for REE sorption onto natural
1060 microbial mats. Chemical Geology, 219, 53–67, 2005.
- 1061 [Tesson, J. and Benedetti, L.: Seismic history from in situ ³⁶Cl cosmogenic nuclide data on](#)
1062 [limestone fault scarps using Bayesian reversible jump Markov chain Monte Carlo.](#)
1063 [Quaternary Geochronology, 52, 1–20, 2019.](#)
- 1064 Tesson, J., Pace, B., Benedetti, L., Visini, F., Delli Roccoli, M., Arnold, M., Aumaître, G.,
1065 Bourlès, D.L. and Keddadouche, K.: Seismic slip history of the Pizzalto fault (central
1066 Apennines, Italy) using in situ-produced ³⁶Cl cosmic ray exposure dating and rare earth
1067 element concentrations. Journal of Geophysical Research: Solid Earth, 121, 1983–2003,
1068 2016.
- 1069 Tikhomirov D., Amiri, N.M., Ivy-Ochs, S., Alifimov, V., Vockenhuber, C., Akçar, N.: Fault
1070 Scarp Dating Tool – a MATLAB code for fault scarp dating using in-situ chlorine-36
1071 supplemented with datasets of Yavansu and Kalafat faults. Data in brief, 26, 104476,
1072 2019.
- 1073 ~~Tesson, J. and Benedetti, L.: Seismic history from in situ ³⁶Cl cosmogenic nuclide data on~~
1074 ~~limestone fault scarps using Bayesian reversible jump Markov chain Monte Carlo.~~
1075 ~~Quaternary Geochronology, 52, 1–20, 2019.~~

- 1076 Tucker, G. E., McCoy, S. W., Whittaker, A. C., Roberts, G. P., Lancaster, S. T. and Phillips,
1077 R.: Geomorphic significance of postglacial bedrock scarps on normal-fault footwalls.
1078 Journal of Geophysical Research: Solid Earth, 116, F01022, 2011.
- 1079 [Vougioukalakis, G.E., Satow, C.G., and Druitt, T.H.; Volcanism of the South Aegean](#)
1080 [Volcanic Arc, Elements, 15, 159–164, 2019.](#)
- 1081 Wallace, R. E.: Grouping and migration of surface faulting and variations in slip rates on
1082 faults in the Great Basin province. Bulletin of the Seismological Society of America, 77,
1083 868–876, 1987.
- 1084 Woodcock, N.H. and Mort, K.: Classification of fault breccias and related fault rocks.
1085 Geological Magazine, 145, 435–440, 2008.
- 1086 Yang, X., Liu, Y., Li, C., Song, Y., Zhu, H. and Jin, X.: Rare earth elements of aeolian
1087 deposits in Northern China and their implications for determining the provenance of dust
1088 storms in Beijing. Geomorphology, 87, 365–377, 2007.
- 1089 Zreda, M. and Noller, J. S.: Ages of prehistoric earthquakes revealed by cosmogenic
1090 chlorine-36 in a bedrock fault scarp at Hebgen Lake. Science, 282, 1097–1099, 1998.

1091 **Table 1:** Parameters for MCMC modelling of slip rate.

α (°)	β (°)	γ (°)	Scarp (cm)	Buried scarp (cm)	ρ_{rock} (g cm ⁻³)	$\rho_{\text{colluvium}}$ (g cm ⁻³)	³⁶ Cl P_o (at. g ⁻¹ yr ⁻¹)	ϵ (mm yr ⁻¹)	Pre (kyr)	Scarp age (kyr \pm 1 σ)	Elapsed time (kyr \pm 1 σ)
32	62	20	650	80	2.6	1.9	59.4 \pm 4.3	0.02	7.7	8.0 \pm 1.5	2.5 \pm 1.0

1092

1093 α is hanging wall colluvial surface dip angle; β is scarp dip angle; γ is the dip angle of the hillslope above the fault scarp; ϵ is
 1094 scarp erosion rate; Pre is pre-exposure **duration**; Scarp age is the initial estimate of exhumation of the oldest (highest) part of
 1095 the scarp; Elapsed time is the estimated duration following the last earthquake. The ³⁶Cl production rate of 59.4 \pm 4.3 at g⁻¹ yr⁻¹
 1096 is taken from Schlagenhauf et al. (2010), **re**-calculated from Lifton et al. (2005).
 1097 When using the ³⁶Cl production rate of 48.8 \pm 3.5 at g⁻¹ yr⁻¹ from Stone et al. (1996), Pre is 10.6 kyr; otherwise, all other
 1098 parameters are fixed.

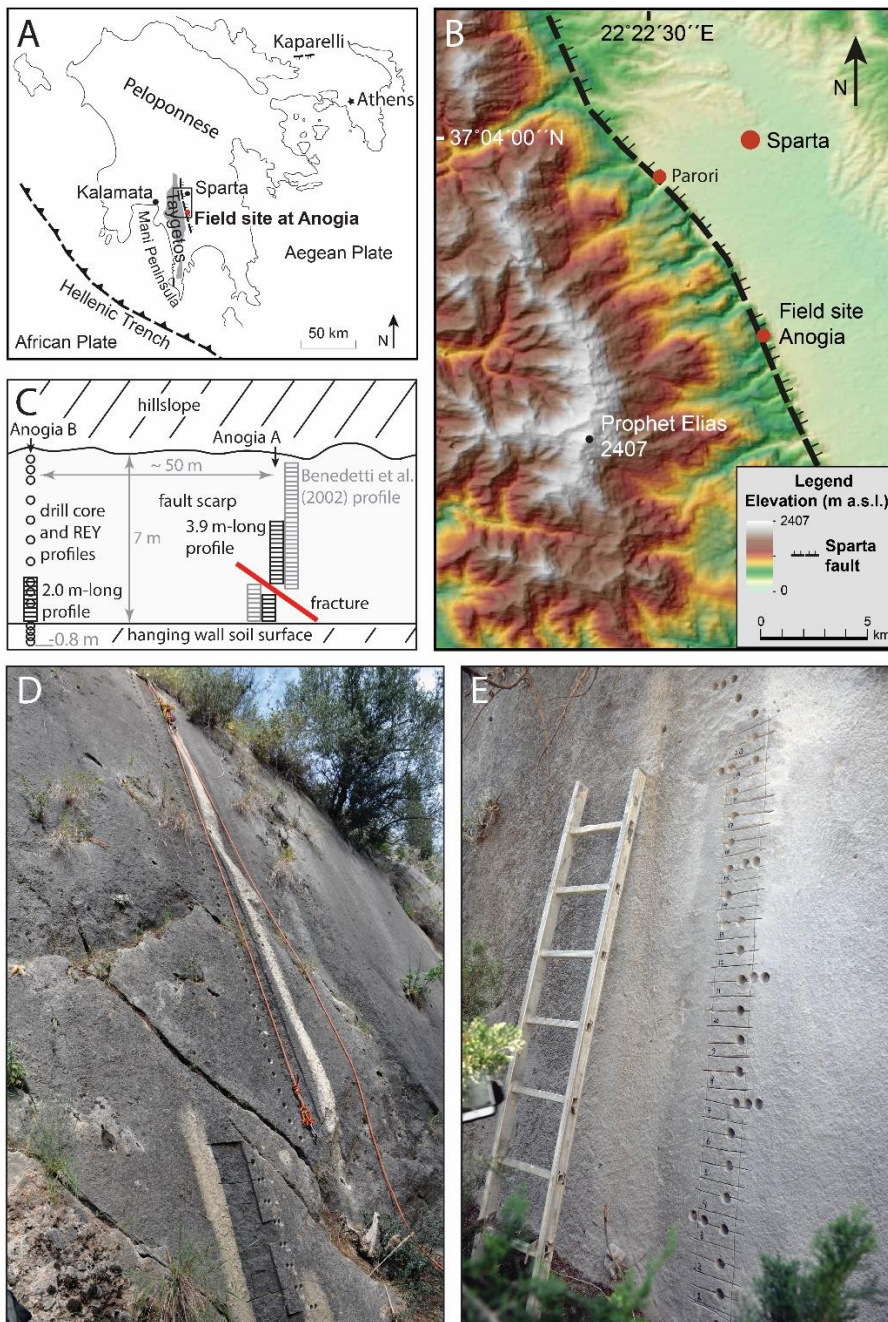
1099

1100 **Table 2:** Slip rates for the Sparta **Ff** fault at Anogia from the best Markov chain Monte Carlo
 1101 models (n = 10,000), for end-member ³⁶Cl production rates and varying number of model
 1102 earthquakes.

Slip rate calculation model (³⁶ Cl production rate, number of earthquakes)	Mean slip rate (mm yr ⁻¹)	MAP slip rate (mm yr ⁻¹)
48.8, 3 earthquakes, to present	0.72	0.70
48.8, 5 earthquakes, to present	0.71	0.70
48.8, 6 earthquakes, to present	0.70	0.70
59.4, 3 earthquakes, to present	0.79	0.76
59.4, 5 earthquakes, to present	0.78	0.75
59.4, 6 earthquakes, to present	0.77	0.75
48.8, 3 earthquakes, to 464 B.C.E. earthquake	1.10	1.08
48.8, 5 earthquakes, to 464 B.C.E. earthquake	1.11	1.11
48.8, 6 earthquakes, to 464 B.C.E. earthquake	1.10	1.11
59.4, 3 earthquakes, to 464 B.C.E. earthquake	1.21	1.15
59.4, 5 earthquakes, to 464 B.C.E. earthquake	1.22	1.16
59.4, 6 earthquakes, to 464 B.C.E. earthquake	1.22	1.18
48.8, 5 earthquakes, 0–3.7 m on fault scarp	0.95	0.94
59.4, 5 earthquakes, 0–3.7 m on fault scarp	1.03	0.96
48.8, 5 earthquakes, 3.7–6.5 m on fault scarp	0.83	0.80
59.4, 5 earthquakes, 3.7–6.5 m on fault scarp	0.92	0.92

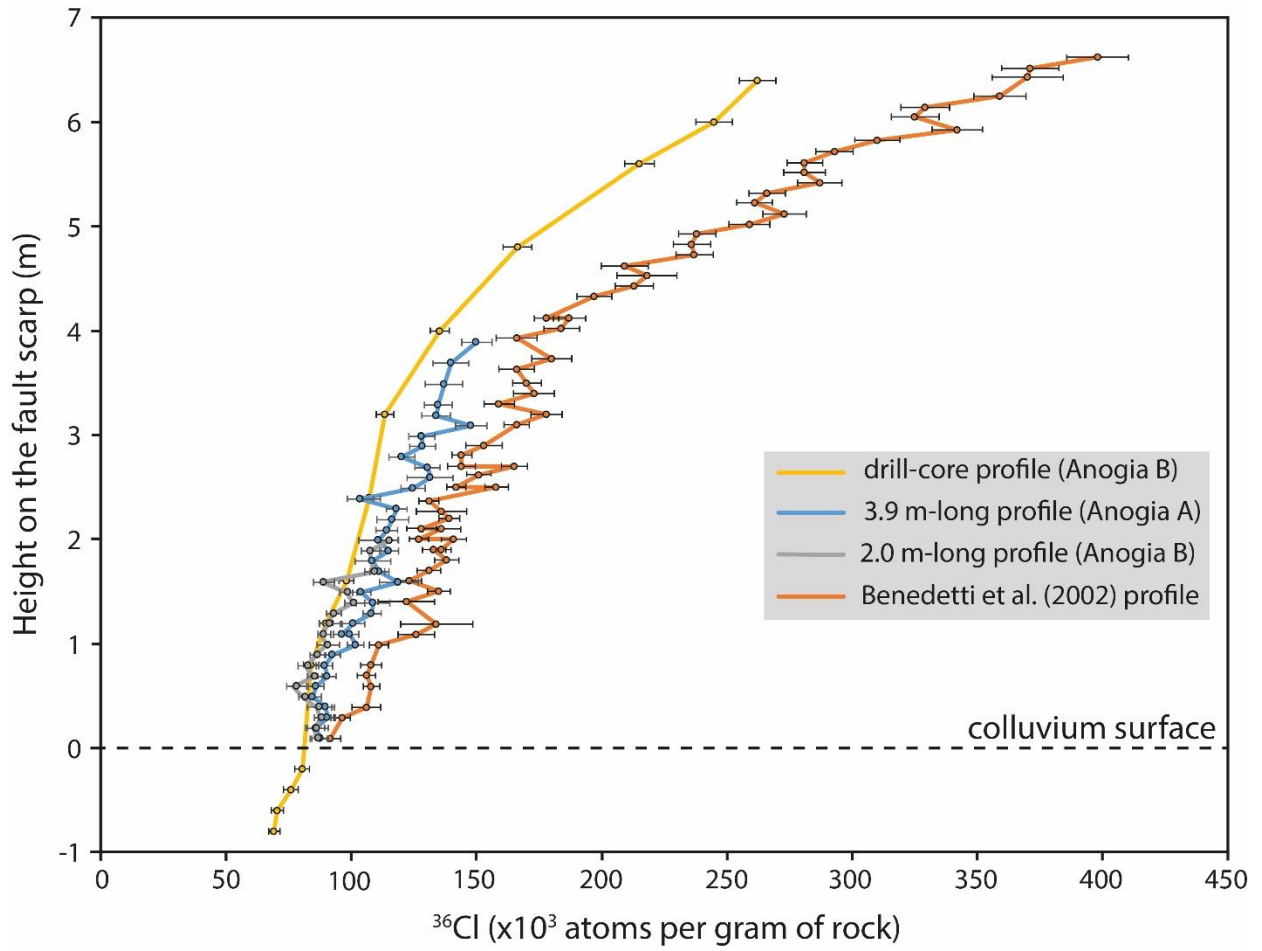
1103

MAP is maximum a posteriori probability



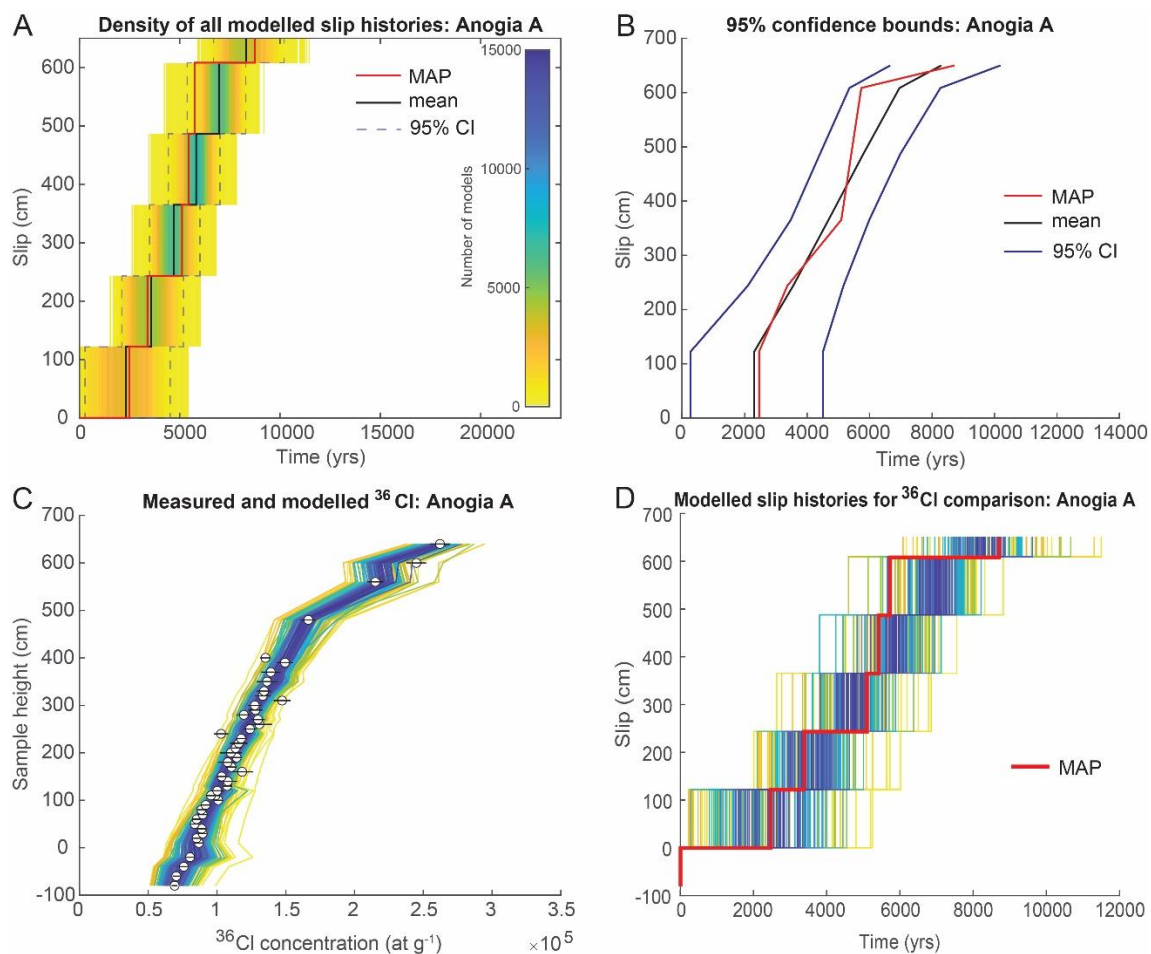
1105

1106 **Fig. 1:** Study site. A. The study site location in Peloponnese, Greece. Key tectonic features
 1107 are shown. Box indicates location of panel B. B. The location of the Sparta **F**fault, separating
 1108 the Taygetos Mountains from the Sparta basin. The location of the Anogia field site used both
 1109 in this study and in Benedetti et al. (2002) is shown. Benedetti et al. (2002) located a second
 1110 sampling transect at Parori (also shown). The digital elevation model has a 24 m resolution
 1111 and is derived from ASTER GDEM (GDEM2), which is a product of NASA and METI
 1112 (Japan). C. Schematic diagram of the Sparta **F**fault scarp at Anogia, showing the locations of
 1113 our vertical ^{36}Cl and REE-Y sampling transects, and the ^{36}Cl sampling transect of Benedetti
 1114 et al. (2002). D. Photograph showing the location of **our 3.9 m-long the Anogia A** profile,
 1115 prior to sampling. The existing sample scar is from Benedetti et al. (2002). E. Photograph
 1116 showing the location of our REE-Y and drill core profiles, after sampling, and **our 2.0 m**
 1117 **long the Anogia B** profile, before sampling.



1118
 1119
 1120
 1121
 1122

Fig. 2: Sparta ~~F~~fault ³⁶Cl concentration profiles. Error bars indicate 1σ measurement uncertainties.-



1123

1124

1125

1126

1127

1128

1129

1130

1131

1132

1133

1134

1135

1136

1137

1138

1139

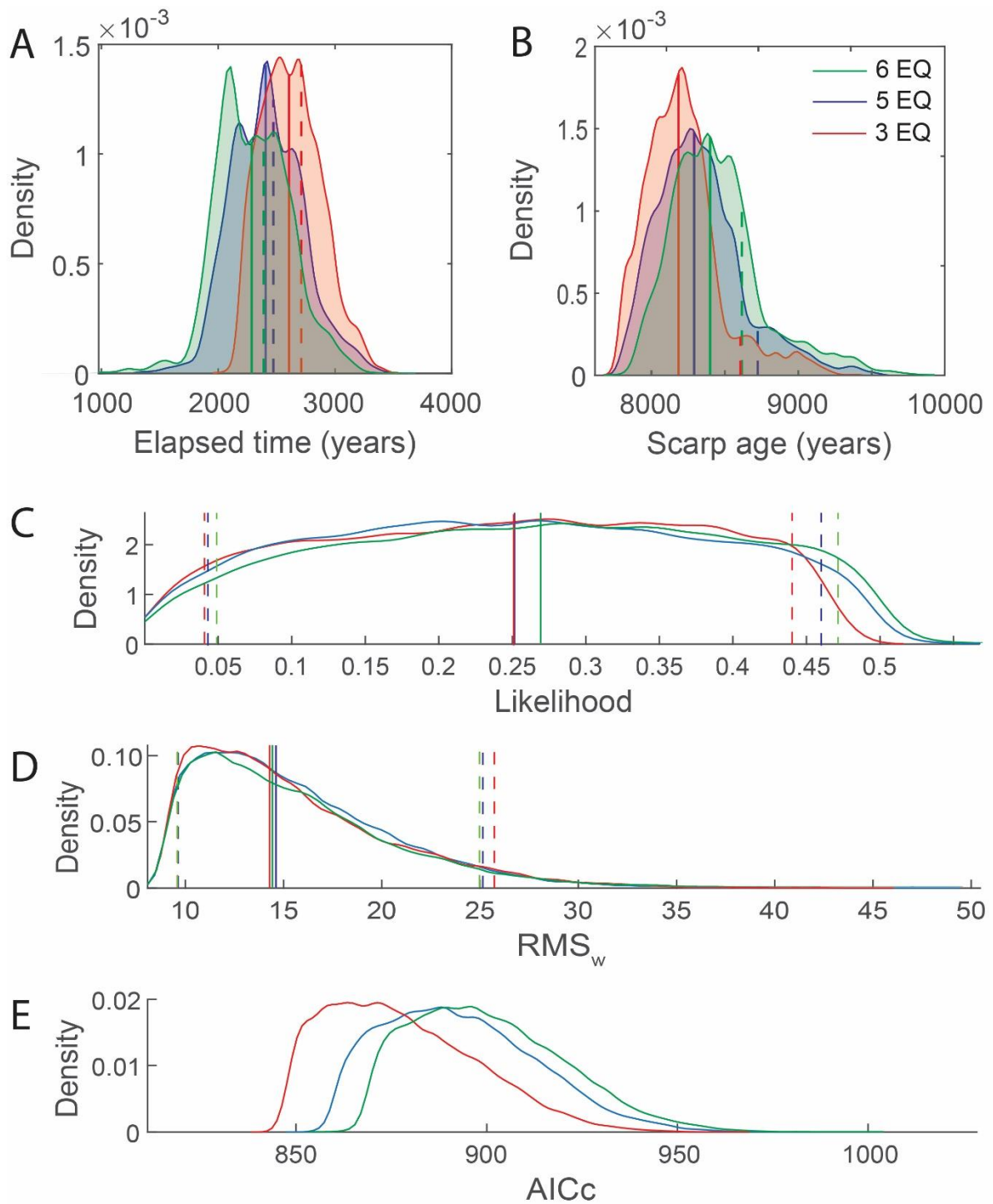
1140

1141

1142

1143

Fig. 3: Markov chain Monte Carlo (MCMC) model fits to measured ^{36}Cl concentrations and model slip histories, Anogia A + drill core profile. Slip accumulation is shown for five model earthquakes that each exhume the same vertical length of scarp rather than reflecting the magnitude and timing of historical earthquakes. The red line in panels a, b, and d is the maximum a posteriori probability (MAP) estimation model, which is the maximum likelihood multiplied by the prior probability based on scarp age. Each panel includes 160k iterations, following removal of a burn-in of the first 40k iterations. A. Histogram showing the distribution of accepted model slip histories in slip-space versus time. The density of overlapping models increases from warm to cool colours. The mean model and 95% confidence bounds are also shown. B. The 95% confidence bounds of the smoothed model distribution (black lines) calculated for age at each step in the slip. The mean (black line) and MAP (red line) slip histories are also plotted. C. Model fits to measured ^{36}Cl concentrations (circles). The coloured lines represent a selection of 160 model fits from low- (yellow) to high-probability (blue) at equal intervals (1000) through the distribution. The black lines indicate 1σ measurement uncertainties. D. Slip histories through five model earthquakes corresponding to MCMC fits shown in panel c. Results are shown for a ^{36}Cl production rate of 59.4 ± 4.3 atoms $\text{g Ca}^{-1} \text{yr}^{-1}$. Refer to Fig. S2 for equivalent results using a production rate of 48.8 ± 3.5 atoms $\text{g Ca}^{-1} \text{yr}^{-1}$.



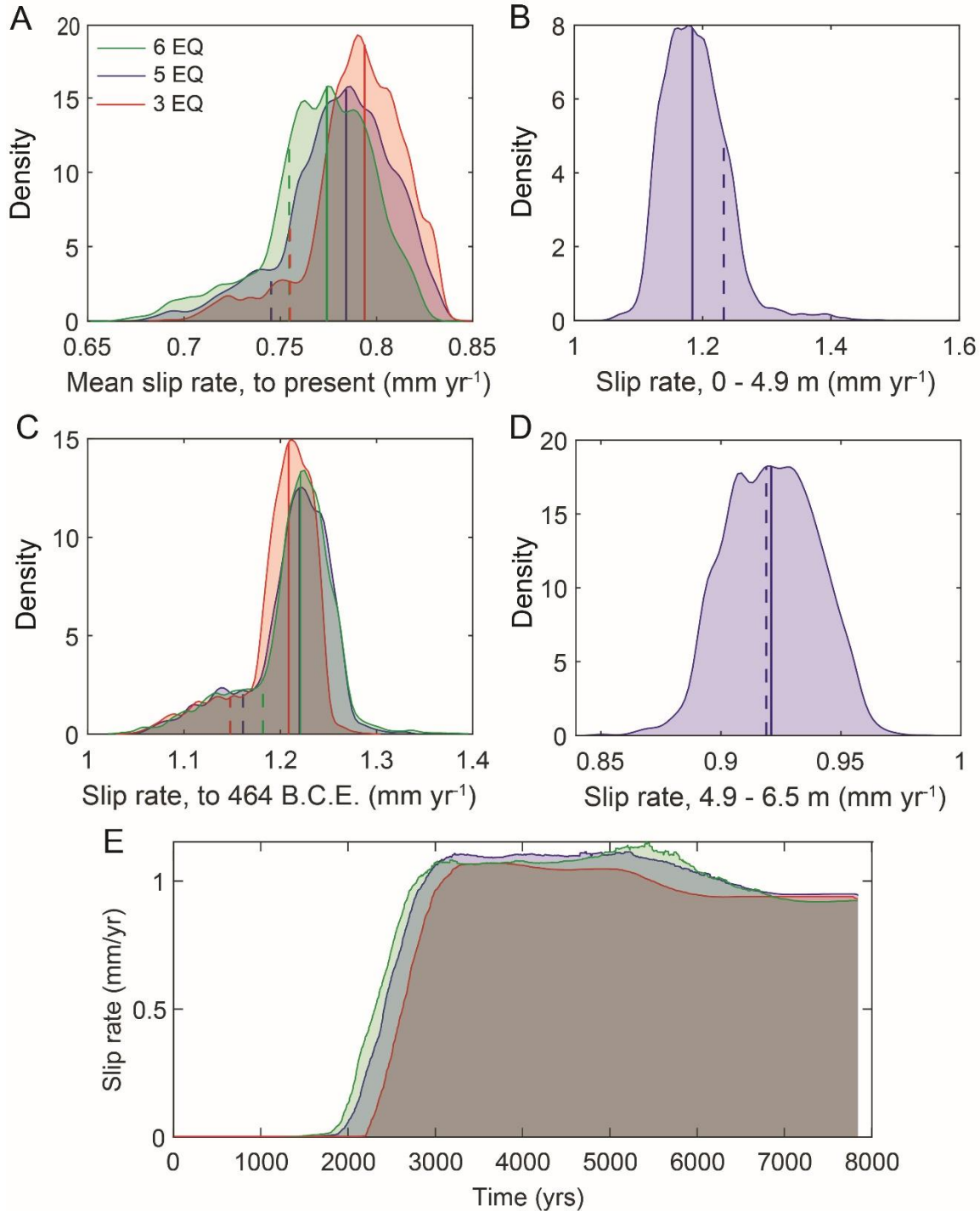
1144
 1145
 1146
 1147
 1148
 1149
 1150
 1151
 1152

Fig. 4: Statistical plots for Markov chain Monte Carlo (MCMC) model iterations. Results are shown for three, five, and six model earthquakes. Vertical red-solid lines indicate the median of each distribution, whereas vertical green-dashed lines indicate 95% confidence intervals, colour-coded according to the number of modelled earthquakes. Posterior probability distribution functions from all models for A. Elapsed Time, and B. Scarp Age. Distributions of C. Likelihood, D. Weighted mean root square (RMS_w), and E. Corrected Akaike's Information Criterion (AICc) of slip history calculated for modelled ³⁶Cl concentrations compared to the measured values. The top 10k models are shown in panels A and B,

1153 whereas panels C, D, and E show statistics for 160k models following removal of a burn-in of
 1154 the first 40k iterations.

1155

1156

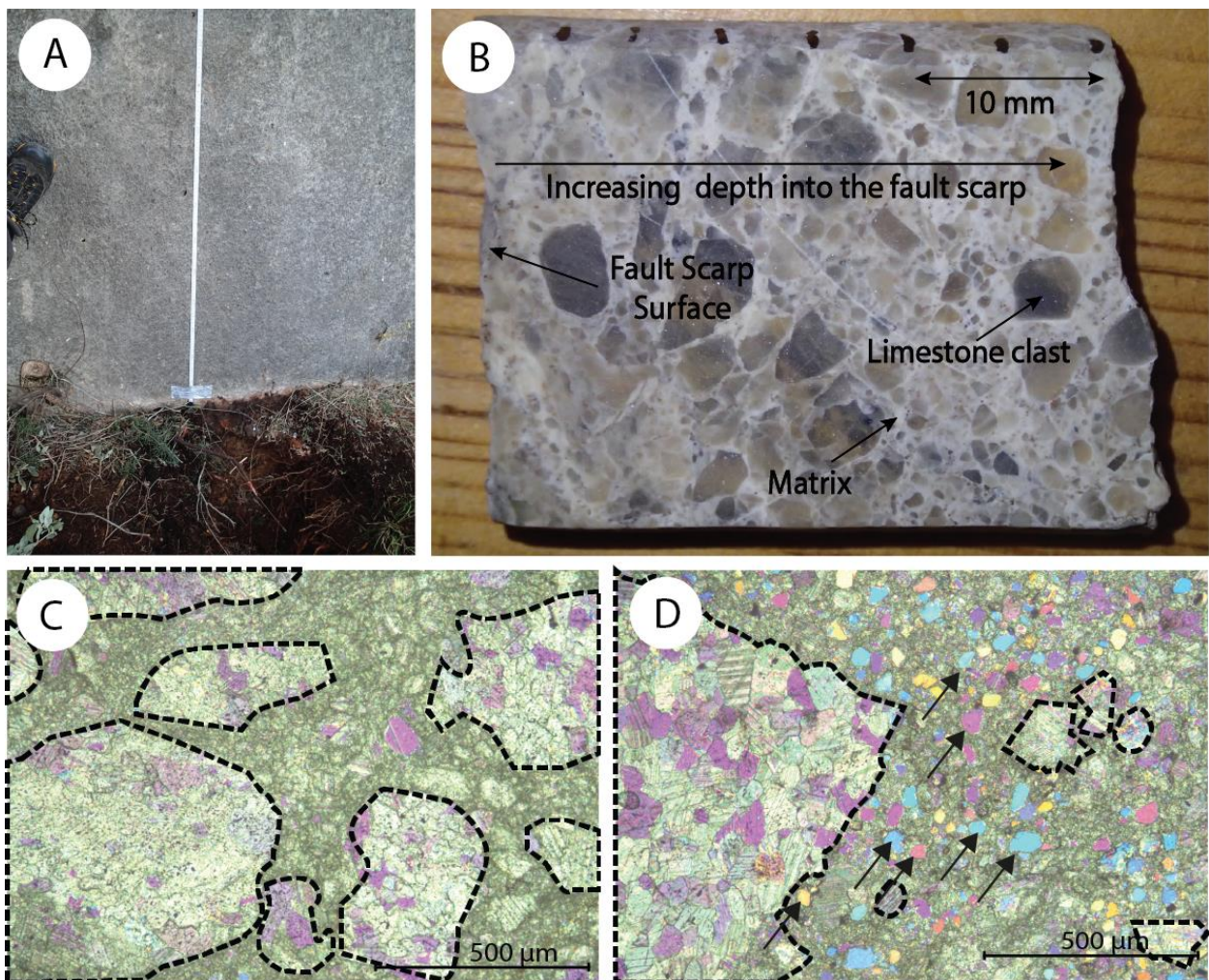


1157

1158 **Fig. 5:** Slip rates for the Sparta Ffault at Anogia (Anogia A plus drill core profile) from
 1159 Markov chain Monte Carlo modelling. Results are shown for three, five, and six model
 1160 earthquakes. In each panel, the most probable (top 6%) models calculated from the median
 1161 scarp age and scarp height are shown. Solid and dashed vertical lines indicate the mean and

1162 maximum a posteriori probability (MAP) estimation for each distribution, respectively. Slip
 1163 rates are shown for three, five, and six model earthquakes, using a ^{36}Cl production rate of
 1164 59.4 ± 4.3 atoms $\text{g Ca}^{-1} \text{yr}^{-1}$. A. The distribution of the most probable slip rate for the entire
 1165 scarp calculated up to the present day. B. The distribution of the most probable slip rate for
 1166 the entire scarp calculated up to the last known earthquake at 464 B.C.E. C. The distribution
 1167 of the most probable slip rate for lower segment of the scarp. D. The distribution of the most
 1168 probable slip rate for the uppermost segment of the fault scarp. E. Mean slip rate over time.
 1169 Slip rates using a ^{36}Cl production rate of 48.8 ± 3.5 atoms $\text{g Ca}^{-1} \text{yr}^{-1}$ are shown in Fig. S2.

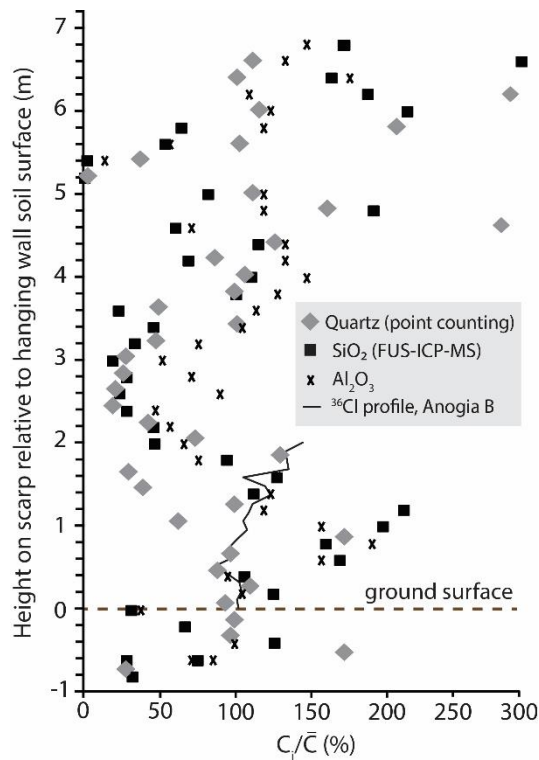
1170
 1171



1172

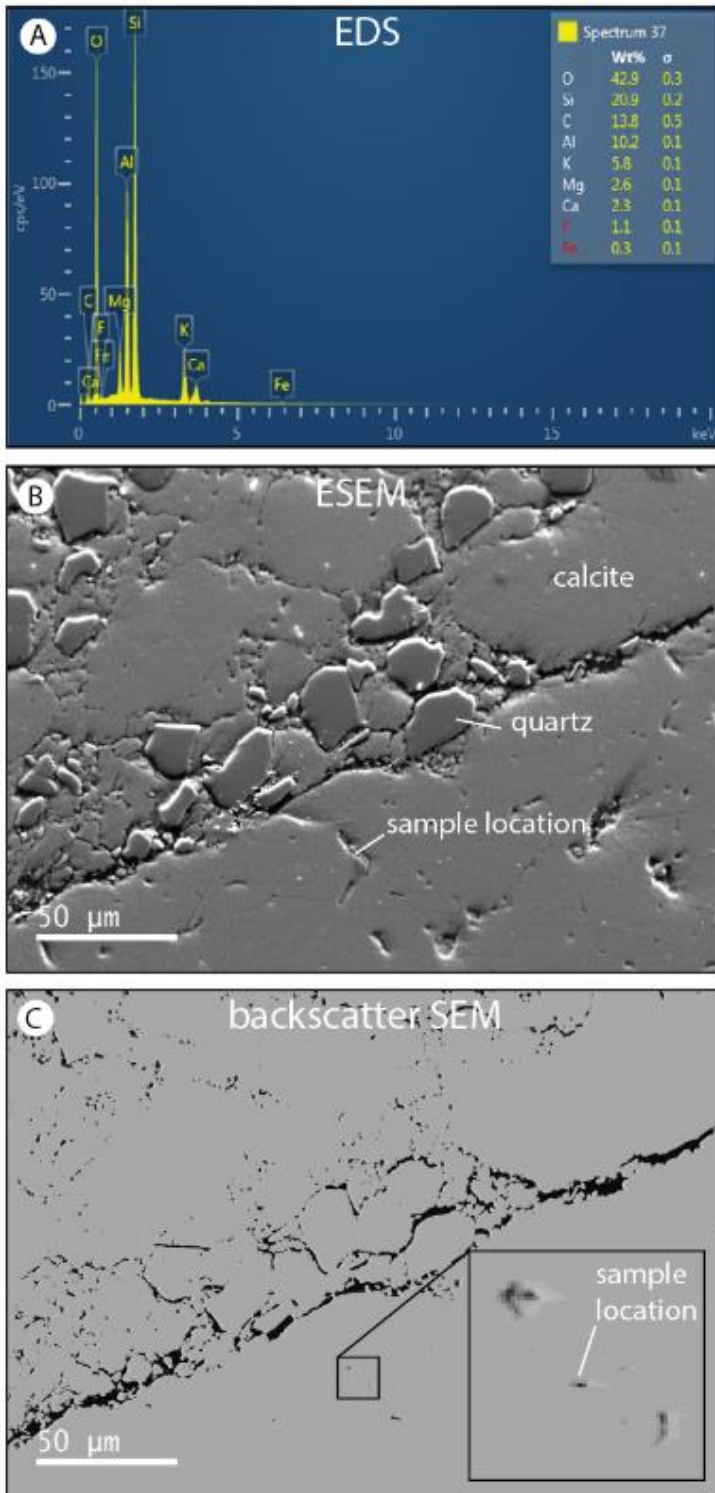
1173 **Fig. 6:** The heterogeneous fault breccia that comprises the Sparta **Ff** fault scarp surface. A. The
 1174 Sparta **Ff** fault scarp surface appears smooth and homogenous, as illustrated by this photograph
 1175 of the scarp base at Anogia (upper half of the dug trench in the foreground). B. Fault breccia
 1176 is revealed in a cut drill core, where clasts of host limestone are cemented in a fine matrix. C.
 1177 A photomicrograph shows limestone clasts (dotted outlines) comprising about 60% of the
 1178 thin section area. D. A photomicrograph shows fine matrix comprising about 60% of the thin
 1179 section area. Arrows indicate quartz.

1180

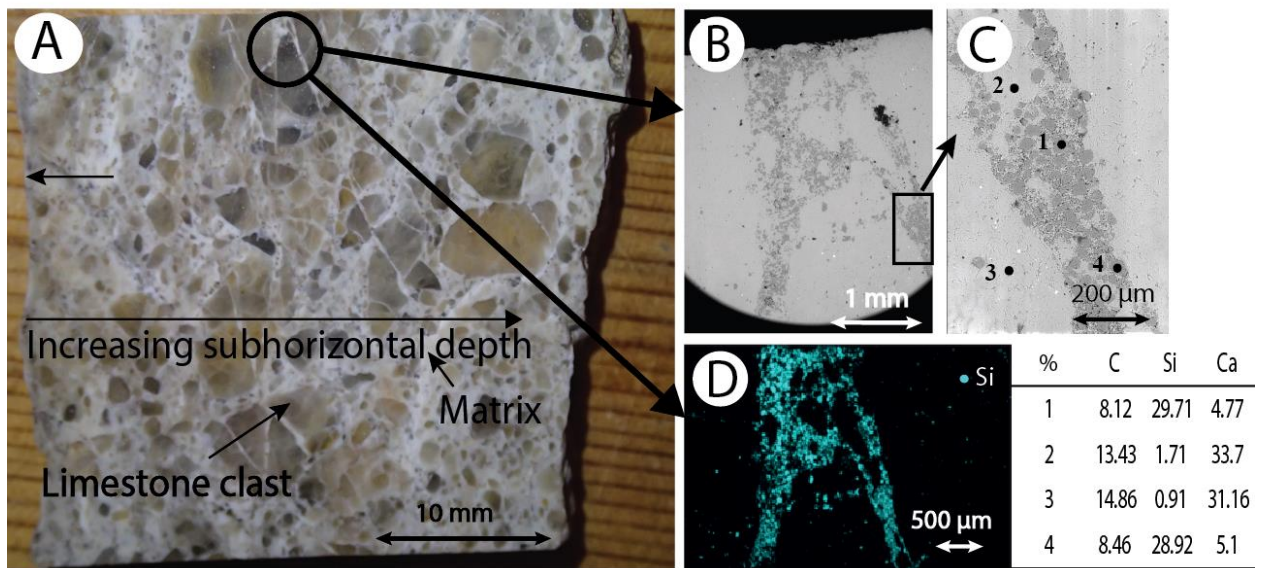


1181
 1182
 1183
 1184
 1185
 1186

Fig. 7: Concentrations of Al₂O₃ and SiO₂, and quartz abundances from point counting, along a vertical profile, Sparta Fault scarp, Anogia. The concentration of each element (C_i) is normalized to its mean concentration through the profile (C_i/\bar{C}). The locations of former soil surface horizons inferred from ³⁶Cl concentrations and from the scarp geochemistry are shown for reference.



1187
 1188 **Fig. 8:** Energy-dispersive X-ray spectroscopy (EDS) elemental abundances, and
 1189 environmental scanning electron microscope (ESEM) and backscatter SEM imagery of a thin
 1190 section of fault breccia comprising the Sparta **F** fault scarp surface at 1.1 m above the hanging
 1191 wall. (A). Element abundances in a pore, the location of which is shown in panels B and C.
 1192 Si, Al, and K are abundant relative to Ca, which indicates that clay, e.g., illite, is lining the
 1193 pore. (B) Quartz is an abundant constituent of the thin section matrix. (C) Porosity, shown in
 1194 black; note its spatial association with quartz. The location of the sample used in panel A is in
 1195 a small pore, shown in the inset.



1197

1198

1199

1200

1201

1202

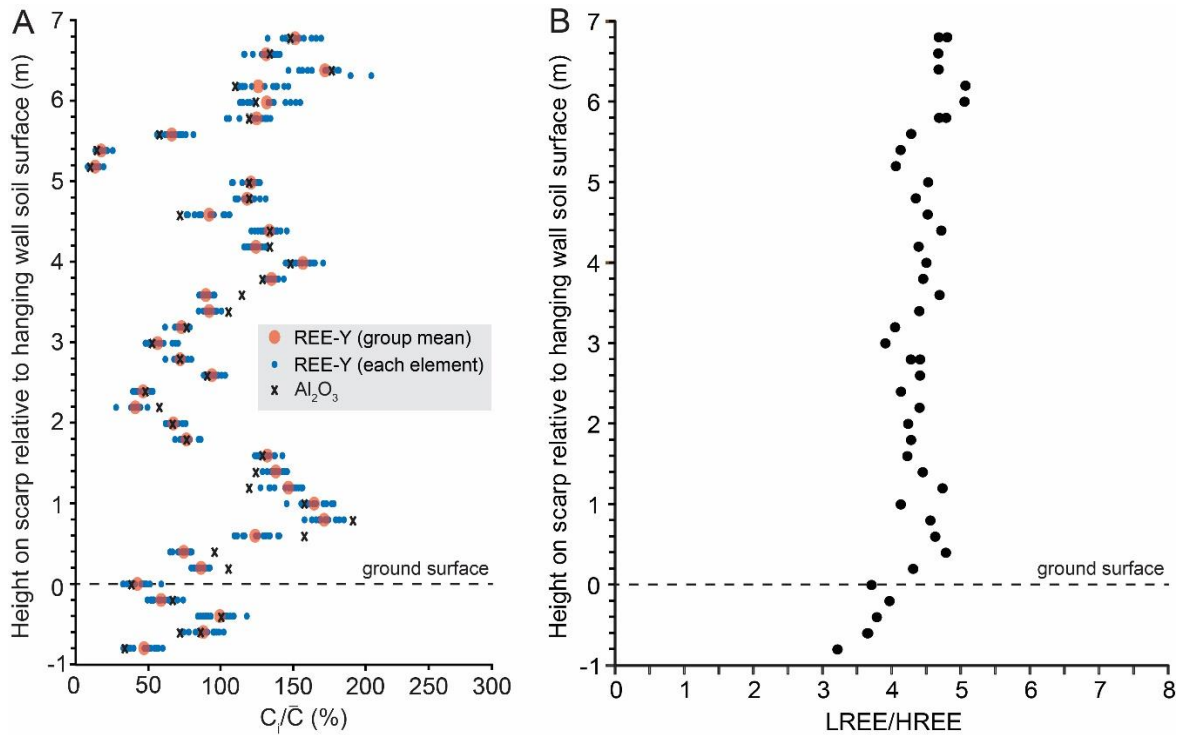
1203

1204

1205

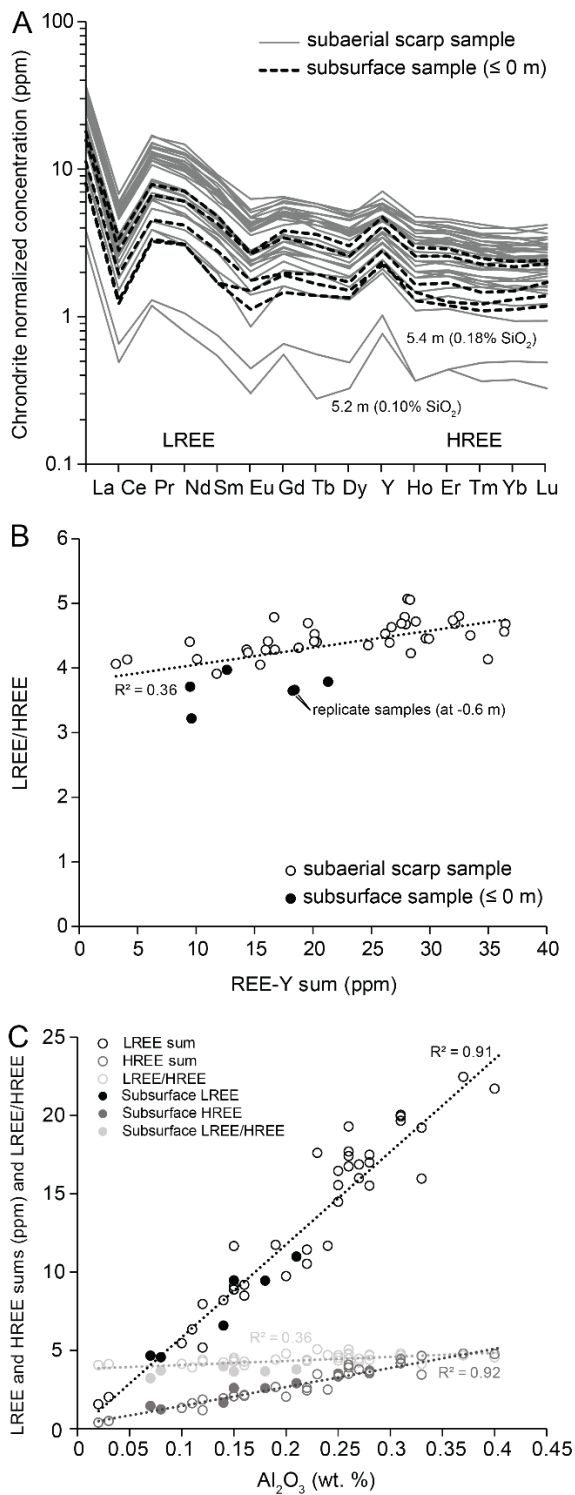
1206

Fig. 9: Concentrations of Si in the Sparta Ffault breccia, 1.1 m above the scarp base at Anogia. A. A cut drill core from the Sparta Ffault scarp at Anogia showing limestone clasts cemented in fine matrix. The circled fine matrix is examined under high resolution in panels B to D. B. An ESEM image showing the sample location for spot elemental analysis (rectangle). C. Sample points for elemental analysis using EDS, with values shown in the table. D. The abundance of Si in the fine matrix illustrated in magenta for the circled part of the thin section shown in panel A.



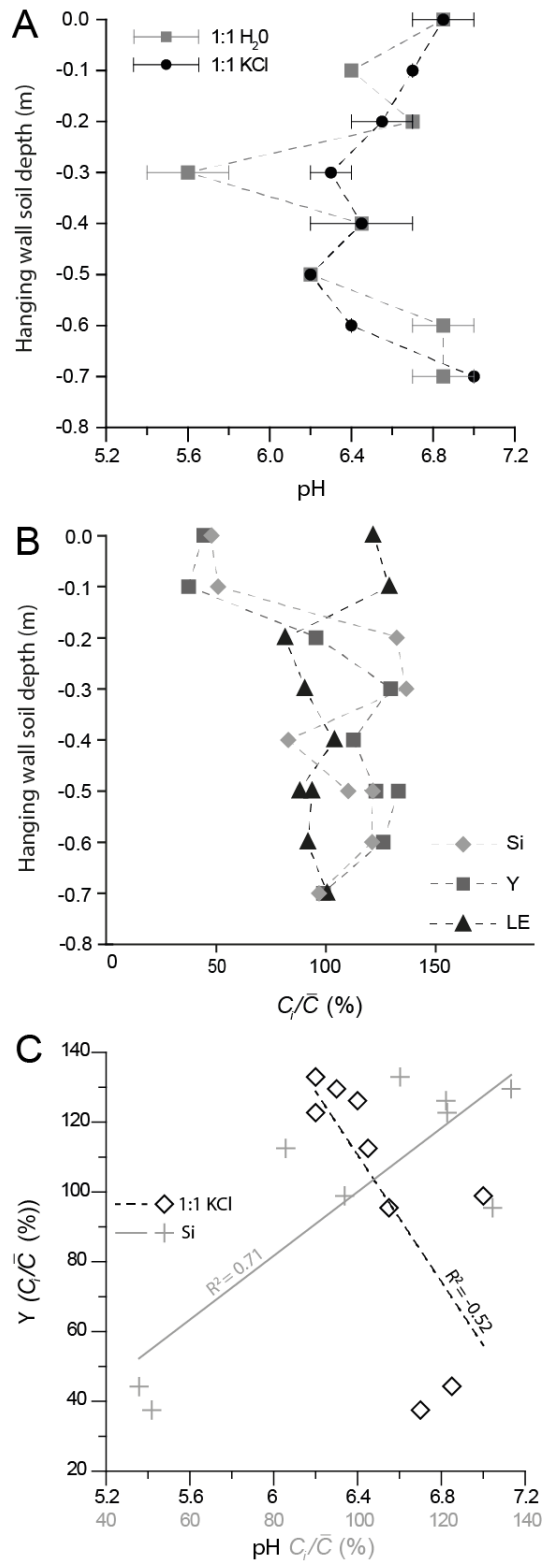
1207
 1208
 1209
 1210
 1211
 1212
 1213
 1214
 1215
 1216
 1217
 1218

Fig. 10: Vertical distribution of REE-Y elements on the Sparta Ffault (Anogia B profile). A. REE-Y concentrations. Mean values for all REE-Y elements at each sample point are shown in red dots, whereas individual REE-Y elements are shown in blue dots. The concentration of each element (C_i) is normalized to its mean concentration through the profile (C_i/\bar{C}). Concentrations of Al_2O_3 and former soil surface horizons inferred from ^{36}Cl concentrations profiles and geochemical data, are shown for reference. B. LREE:HREE ratio. There are two measurements at -0.6 m.



1219
 1220
 1221
 1222
 1223
 1224
 1225
 1226
 1227

Fig. 11: REE-Y elements on the Sparta Fault (Anogia B profile). A. Concentrations of rare-earth elements and yttrium (REE-Y) normalized to chondrite composition (McDonough and Sun, 1995). Each line shows a measured location on the scarp surface. The two low REE-Y outliers at 5.2 m and 5.4 m also have exceptionally low SiO_2 and Al_2O_3 . B. LREE:HREE versus REE-Y sum. The R^2 value is for a linear fit. C. LREE, HREE, and LREE:HREE versus Al_2O_3 (wt.%). The R^2 values are for linear fits. In each panel, the six subsurface samples (≤ 0 m), including a replicate measurement at -0.6 m.



1229

1230

1231

1232

1233

1234

1235

1236

Fig. 12: Hanging wall soil chemistry, adjacent to the Sparta **F** fault scarp at Anogia. A. Soil pH along a vertical profile measured from soil mixed with distilled H₂O and 1M KCl. Uncertainty ranges show the ≤ 0.5 resolution of the indicator strips. B. Concentrations of Si, Y, and elements too light to be measured using handheld XRF (LE, including C) along the vertical soil profile. Each element has been normalized through division by its mean concentration through the soil. C. Y concentrations plotted against pH (measured from 1:1 KCl) and Si concentration at each measured depth interval beneath the soil surface.